nature communications

Article

https://doi.org/10.1038/s41467-024-53700-9

Induction of a distinct macrophage population and protection from lung injury and fibrosis by Notch2 blockade

Received: 29 August 2023

Accepted: 20 October 2024

Mayra Cruz Tleugabulova [1,11], Sandra P. Melo [2,11] ✉, Aaron Wong[3], Alexander Arlantico[3], Meizi Liu [4], Joshua D. Webster[5], Julia Lau[6], Antonie Lechner [7], Basak Corak [7], Jonathan J. Hodgins [8], Venkata S. Garlapati[8], Marco De Simone[6], Ben Korin [8], Shimrit Avraham [8], Jessica Lund[6], Surinder Jeet[3], Alexander Reiss[3], Hannah Bender[5], Cary D. Austin[5], Spyros Darmanis[6], Zora Modrusan[6], Hans Brightbill[3], Steffen Durinck[2], Michael S. Diamond [4,9,10], Christoph Schneider [7], Andrey S. Shaw [8] ✉ & Maximilian Nitschké [8] ✉

Macrophages are pleiotropic and diverse cells that populate all tissues of the body. Besides tissue-specific resident macrophages such as alveolar macrophages, Kupffer cells, and microglia, multiple organs harbor at least two subtypes of other resident macrophages at steady state. During certain circumstances, like tissue insult, additional subtypes of macrophages are recruited to the tissue from the monocyte pool. Previously, a recruited macrophage population marked by expression of *Spp1, Cd9, Gpnmb, Fabp5*, and *Trem2*, has been described in several models of organ injury and cancer, and has been linked to fibrosis in mice and humans. Here, we show that Notch2 blockade, given systemically or locally, leads to an increase in this putative pro-fibrotic macrophage in the lung and that this macrophage state can only be adopted by monocytically derived cells and not resident alveolar macrophages. Using a bleomycin and COVID-19 model of lung injury and fibrosis, we find that the expansion of these macrophages before lung injury does not promote fibrosis but rather appears to ameliorate it. This suggests that these damage-associated macrophages are not, by themselves, drivers of fibrosis in the lung.

Macrophages are present in every tissue and play important roles in tissue homeostasis as well as in coordinating the immune system response to pathogens and tissue injury. Macrophages are extremely diverse, with distinct ontogenies, tissue-specific phenotypes, and diverse functions in inflammation and repair[1,2]. While originally believed to be derived from blood monocytes, it is now known that some tissue-specific resident macrophages, for example microglia, Kupffer cells, alveolar macrophages, and Langerhans cells are embryonically derived and self-replenish throughout life[3–8]. Recent studies show that many organs harbor additional tissue macrophages that can be broadly defined into two or three different subsets[9]. While the exact function of different tissue macrophage subsets is not fully understood, they are implicated to function in promoting tissue inflammation, tissue repair, and aberrant responses like tissue fibrosis[10–13].

In the lung, the classical tissue-resident macrophage is the alveolar macrophage, which resides in the lumen of the alveoli. Within the parenchyma of the lung, an additional tissue macrophage called the interstitial macrophage (IM) can be found close to the vasculature

A full list of affiliations appears at the end of the paper. ✉e-mail: melocars@gene.com; shawa6@gene.com; nitschkm@gene.com

and the large airways, and within the interstitium of the alveolar walls[12,14–16]. Multiple studies using surface markers, bulk, and single-cell RNA-seq show that IMs can be divided into two or three subsets[12,14,16].

The Notch pathway plays a critical role in cell differentiation in many systems including myeloid cells[17–22]. There are four Notch receptors, Notch1-4, that interact with five different ligands, Jag1,2, Dll1, 3, 4. In myeloid cells, Notch2 signaling is known to be critical for the development of the Esam$^+$ Type 2 conventional dendritic cell (cDC2)[17,19] and for the conversion of Ly6C^{hi} classical monocytes to Ly6C^{lo} patrolling monocytes[22]. In the spleen and heart, this conversion also inhibits monocyte recruitment into tissue and subsequent macrophage differentiation[22,23].

In this work, we test whether Notch2 functions in the development and homeostasis of IMs in the lung using Notch2 blocking antibodies administered either systemically (intraperitoneally, IP), or locally (intratracheally, IT). We find that both systemic and local Notch2 blockade increases the number of IMs in the lung. Single cell RNA sequencing (scRNAseq) shows that Notch2 blockade expanded a population of macrophages not prevalent in the steady state. Interestingly, these macrophages developed from monocytes but acquired slightly different phenotypes depending on systemic or local antibody administration, respectively. These macrophages expressed *Spp1, Cd9, Gpnmb, Fabp5*, and *Psap*, all genes associated with macrophages in lung fibrosis in mice and humans[24–27]. Using our dataset as a reference, we searched a wide variety of public scRNAseq datasets and find that macrophages with a similar phenotype are indeed present in injury and disease settings in a variety of tissues. However, pre-treatment with αNotch2 antibodies to expand these cells did not worsen fibrosis after bleomycin injury or after COVID infection, but instead significantly ameliorates it. This suggests that macrophages with this phenotype did not potentiate the fibrosis response and may function protectively.

Results

Notch2 inhibition enhances the number of interstitial lung macrophages

Only Notch1 and Notch2 have significant transcriptional expression in macrophages, with Notch2 expressed more than 10-times higher than Notch1 (Supplementary Fig. 1a). To test whether Notch2 signaling regulates lung interstitial macrophages (IM) differentiation, we used blocking antibodies for Notch 1 and Notch2[28] and administered them, intraperitoneally (IP), once per week, for two weeks before analysis at day 14 (Supplementary Fig. 1b). Consistent with previous findings using genetic tools to regulate Notch2 signaling, we observed the loss of Esam$^+$ cDC2s in the spleen[17,19] and the loss of Ly6C^{lo} CD11c$^+$ patrolling monocytes[22,23] (Supplementary Fig. 1 c,d). αNotch2 treatment did not significantly change macrophage numbers in the kidney, liver, and peritoneum, but changes were noted in the spleen, heart, and lung (Fig. 1a, Supplementary Fig. 1e). In the lung, we noted a three to five-fold increase in IMs (Fig. 1b,c). This was specific to blockade of Notch2 as IP administration of Notch1 inhibitor antibodies led to only a small decrease in the number of IMs and alveolar macrophages (AMs) (Fig. 1b,c). The effect of Notch2 blockade on IM numbers was transient as 21 days after the second antibody dose, the level of macrophage expansion was diminished by about half (Fig. 1d).

Notch2 is required for goblet cell transdifferentiation and the formation of inflammatory ILC2s in the lung[29,30]. To confirm that the expansion of IMs was cell intrinsic and not secondary to Notch2 signaling in other cells, we generated bone marrow chimeras that allowed inducible deletion of Notch2 in either the hematopoietic or the non-hematopoietic compartment (Fig. 1e, f). Deletion of Notch2 increased numbers of IMs only when Notch2 was deleted in bone marrow donor cells, suggesting that the effect of Notch2 on IMs was intrinsic to the hematopoietic compartment (Fig. 1e). To confirm that the effect of Notch2-blockade was intrinsic to the macrophage-lineage, we assessed IM numbers in mixed bone marrow chimeras. The bone marrow of WT mice was mixed in a 1:1 ratio, either with bone marrow from control or Rosa26^{CreERT2}Notch2$^{flox/flox}$ mice, and transferred into lethally irradiated WT mice. Congenic marking was used to track the origin of the myeloid cells (Fig. 1g). After tamoxifen treatment, only IMs derived from Notch2 deleted bone marrow were increased in numbers in the lung (Fig. 1g). Thus, Notch2 blockade acts intrinsically on monocyte/macrophage lineage cells to expand IM numbers in the lung.

Single cell analysis of IMs in the steady state and after Notch2 blockade

Recently, several groups using flow cytometry, bulk, and single cell RNA sequencing have reported distinct subpopulations of IMs[9,12,14–16]. To test whether loss of Notch2 signaling has an impact on the distribution of IM subtypes, we sorted populations of IMs, monocytes, and alveolar macrophages and analyzed them using single cell RNA sequencing (scRNASeq) (Supplementary Fig. 2a, b). As the differential expression of MHCII, LYVE-1, CD206 and SiglecF can be used to distinguish among different IM subtypes, AMs, and monocytes, we also included oligonucleotide labeled antibodies to assess surface protein levels of these markers (CITE-seq) (Supplementary Fig. 2c)[9,12,14–16]. Lastly, to differentiate between cells that were in the vasculature versus those in the tissue, an allophycocyanin (APC)-conjugated αCD45 antibody was injected intravenously shortly before euthanizing the mice. An oligonucleotide-labeled αAPC antibody allowed us to distinguish tissue vs. intravascular cells.

A total of ~26,000 cells remained after standard processing and quality control, and were annotated using SingleR and the ImmGen database as reference (Supplemental Fig. 2d)[31]. A total of 4.5% (~1100) of cells were not monocytes or macrophages and were removed from further analysis. Single cell transcriptional profiles of cells treated with control or αNotch2 antibodies were integrated into a single unbatched dataset, scaled by read depth, subjected to principal component analysis (PCA), and visualized in two dimensions using the Uniform Manifold Approximation and Projection method (UMAP). Cells were segregated into three groups annotated as AMs, IMs, and monocytes using the ImmGen database, validating our FACS sorting strategy (Supplementary Fig. 2d).

Clustering analysis was performed to identify distinct subpopulations. This revealed four monocyte clusters (M1, M2, M3, M4), three AM clusters (A1, A2, A3), and four IM clusters (I1, I2, I3, I4) (Fig. 2a). Clusters M4, A2 and I4 were present mainly in αNotch2-treated mice, while M2 was exclusive to control antibody-treated mice (Fig. 2a, b). Interestingly, the M4 population was positioned in the UMAP between monocytes and emergent cluster I4, suggesting that M4 may represent an intermediate population (Fig. 2a).

To find marker genes for each sub-cluster, gene expression profiles were aggregated and tested for differential expression (see methods). Cluster M2 expressed genes consistent with Ly6c^{lo} patrolling monocytes (Fig. 2c, Supplementary Fig. 2e). The absence of M2 cells after Notch2 blockade was consistent with the dependence of Ly6C^{lo} monocytes on Notch2 signaling[22]. Notch2 blockade also induced a shift in the phenotype of AMs from A1 to A2. A2 AMs were characterized by higher expression of *Car4*, a key AM identity marker gene[32], but had similar levels of the AM marker SiglecF by RNA and antibody labeling (Fig. 2c, Supplementary Fig. 2f). A smaller population present in both conditions, A3, was identified as proliferating AMs (Fig. 2c, Supplementary Fig. 2e). Finally, almost all of the IMs in the control mice segregated into clusters I1, I2 and I3. Cluster I1 expressed *Lyve1*, *Folr2*, *Mrc1*, *CD163*, and *CD209f* (Fig. 2c), and was labeled by LYVE-1 and CD206 antibodies (Supplementary Fig. 2c). I1 is consistent with the Lyve1^{hi}MHCII^{lo} subset by Chakarov et al.[12], the CD206$^+$ subset by Schyns et al.[16], the IM1 subset by Gibbings et al[14], or the TLF$^+$ subset by Dick et al.[9]. Cluster I2 was characterized by the expression of *Cx3cr1*, *Cst3*, complement factors (*C1qb*, *C1qa*), and class II related genes (*Cd74*, *H2-Ab1*, *H2-Eb1*), while cluster I3 contained cells with higher

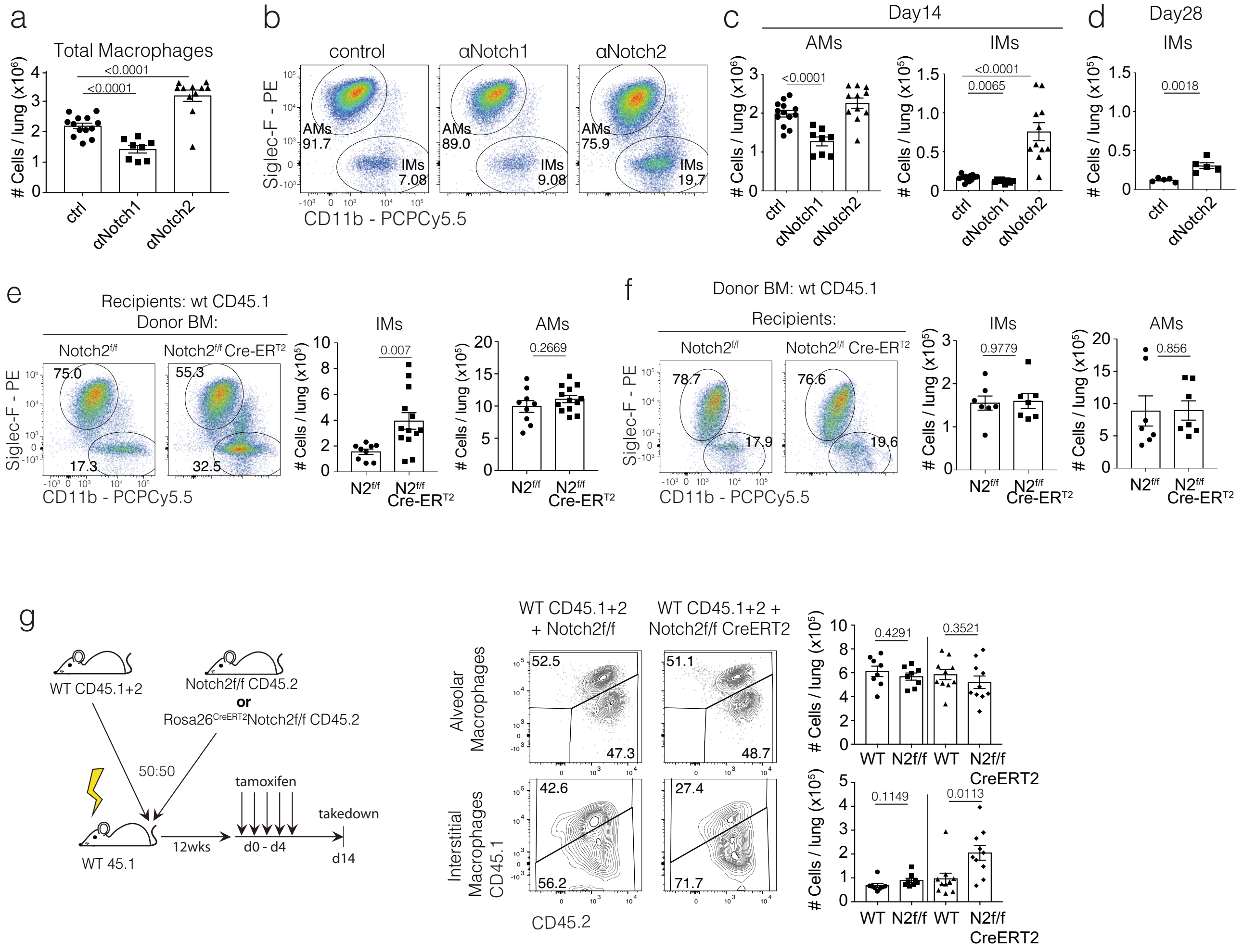

Fig. 1 | Notch2 but not Notch1 inhibition expands lung interstitial macrophages. a–d Analysis of lung macrophages after intraperitoneal (IP) administration of 20 mg/kg of αRagweed (control), αNotch2 or αNotch1 antibodies once per week for two weeks and analyzed at day 14 (a-c) or at day 28 (**d**). Mononuclear cells were isolated and analyzed by flow cytometry for a total number of macrophages ($CD64^+MerTK^+$ cells) (**a**), as well as the proportion and number of alveolar ($CD64^+MerTK^+$ $SiglecF^+/CD11b^{int}$) vs interstitial ($CD64^+MerTK^+$ $SiglecF^-/CD11b^+$) subsets after Notch1 or Notch2 antibody blockade (**b**, **c**). *n* = 13, 3 experiments. **d** Absolute numbers of AMs and IMs after 28 days of αNotch2 antibody blockade (20 days after the last antibody dose). *n* = 5, 1 experiment. **e**, **f** The Notch2 effect is intrinsic to the hematopoietic compartment. Bone marrow from CD45.2 mice expressing either $Notch2^{f/f}$ or $Notch2^{f/f}Cre^{ERT2}$ was used to generate bone marrow chimeras with CD45.1 mice as the hosts, n = 9 $Notch2^{f/f}$-> WT, *n* = 13 $Notch2^{f/f}Cre^{ERT2}$ -> WT, 3 experiments (**e**) as well as the converse *n* = 7 WT -> $Notch2^{f/f}$, *n* = 7 WT-> $Notch2^{f/f}Cre^{ERT2}$, 2 experiments (**f**). **g** Mixed bone marrow chimeras demonstrate that the Notch2 effect is cell intrinsic. Congenically marked WT (CD45.1/2) bone marrow cells were mixed together with $Notch2^{f/f}$ or $Notch2^{f/f}Cre^{ERT2}$ bone marrow (CD45.2) in equal ratios, and transferred intravenously (i.v.) into wild-type mice (CD45.1) as diagrammed in the left panel. After tamoxifen treatment, flow cytometry was used to analyze the contribution of each bone marrow (45.1/2 vs 45.2) to AMs (upper middle panel) and IMs (lower middle panel). The absolute number of alveolar and interstitial macrophages per lung is shown in the right panel. *n* = 10, 2 experiments. An unpaired parametric two-tailed t-test was applied in all graphs where statistical data is shown. Data is graphed as the mean +/- standard error of the mean (SEM).

expression of *Fxyd5* and *Bcl2a1d* (Fig. 2c). I2 and I3 most likely reflect the MHC^{hi} and $CCR2^+$ IM subsets, respectively, as described by Dick and colleagues[9], or one combined population described as $Lyve1^{lo}MHCII^{hi}$ subset by Chakarov et al.[12] or $CD206^-$ subset by Schyns et al.[16].

In contrast, over 80% of IMs from IP αNotch2-treated animals were represented by cluster (I4) (Fig. 2a, b). This population expressed several alternative activation-associated genes such as *Arg1* and *Chil3*, as well as *Spp1*, *Fabp5*, *Gpnmb*, *S100a6*, and multiple cathepsins (*Ctsb, Ctsd, Ctsk, Ctss*) (Fig. 2c). Interestingly, the A2 and M4 populations also expressed some of those markers but to a lesser extent. None of these genes were highly expressed in steady-state IMs (Supplementary Fig. 2e).

To measure the similarity among the populations, we calculated the cosine similarity on the PCA space aggregating the cells by cluster (Fig. 2d). This analysis revealed that even though A2 AMs express some I4 marker genes, A2 AMs were only marginally similar to I4 IMs and grouped firmly with the AMs in clusters A1 and A3. Cluster I4 was the most dissimilar of the clusters, but still grouped with the IM clusters. In summary, systemic Notch2 blockade expanded a population of IMs that were transcriptionally different but still related to IM populations described in the steady state.

Monocytic origin of αNotch2 expanded interstitial macrophages

The induction of the M4 population by Notch2 blockade and its position in the UMAP between monocytes and IMs suggested that the I4 population derived from monocytes. M4 cells were identified as monocytes by both our FACS gating strategy and SingleR using the Immgen database (Supplementary Fig 2d), but did not label with the αCD45-APC antibody used to mark intravascular cells (Fig. 3a). Cosine similarity analysis showed that M4 monocytes shared similarities with

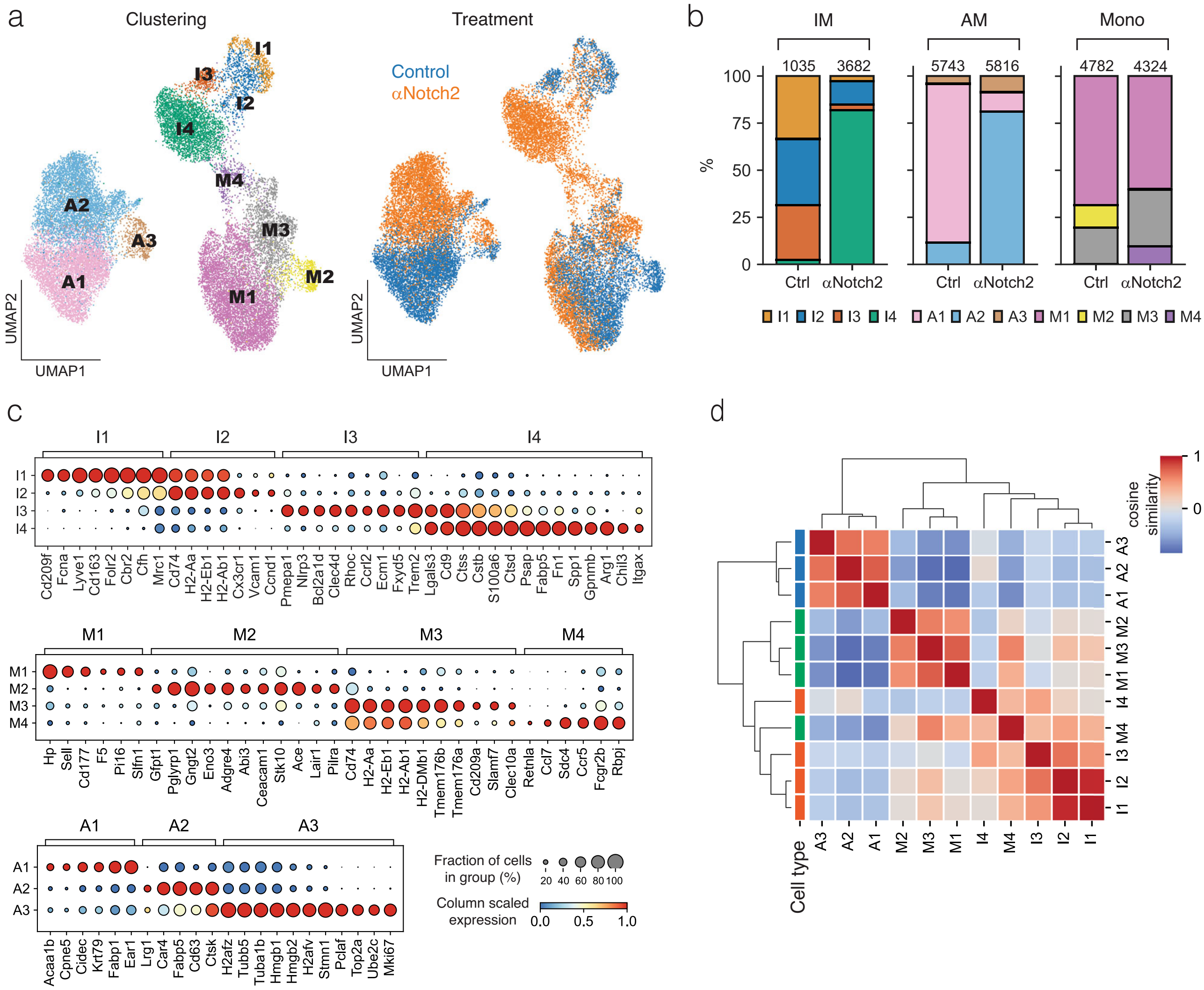

Fig. 2 | Notch2 inhibition expands a population of Spp1, Gpnmb, Fabp5 expressing macrophages in the lung. a scRNAseq analysis of sorted monocytes, AMs, and IMs from mice treated IP with αNotch2 (2 mice) or control antibody (4 mice), shown as a UMAP with clusters generated by unsupervised clustering. Cells, colored on the basis of antibody treatment, are shown on the right. **b** The distribution of cells (IMs – left, AMs – middle, monocytes – right) comparing the effect of αNotch2 antibody treatment as a percentage of the total. **c** Bubble plots show differentially expressed genes identified as markers for each population. Their average expression is normalized across columns (color-coded), and the percentage of cells expressing the genes within each cluster is shown by the size of the bubble. **d** Clustermap depicting pairwise cosine similarities between each of the defined clusters shows high similarity of the M4 cluster to IMs and monocytes.

I4 macrophages as well as the steady-state IMs (Fig. 2d). To investigate the origin of the emerging I4 population, we leveraged the presence of spliced and unspliced RNA molecules in the scRNAseq data to infer cell transitions and trajectories using RNA velocity[33] (Supplementary Fig. 3a). The transcriptional profiles of the IM, AM and monocyte populations were integrated according to treatment, and velocity vectors were calculated after removing genes with less than 20 shared unspliced/spliced counts[33]. In control mice, we did not identify any cell transitions between the three main cell types (IM, AM, monocyte, Fig. 3b, Supplementary Fig. 3b), suggesting that AMs and IMs are relatively stable populations and that any potential replacement by monocytes is a rare and/or slow process. After Notch2-blockade, however, we readily identified cell transitions between monocytes and the expanded αNotch2-derived IM cluster I4 but not from AMs (Fig. 3b).

To experimentally validate the monocytic origin of IP αNotch2-derived IMs we used mice lacking the CCR2 receptor. CCR2 is required for monocyte egress from the bone marrow and CCR2 deficient mice have reduced numbers of monocytes in the blood[34,35]. αNotch2 treatment of CCR2 KO mice showed an attenuated expansion of IMs, confirming that monocytes were a main contributor to the expanded interstitial macrophage population after Notch2 blockade (Fig. 3c).

Local Notch2 blockade induces I4 macrophages with alveolar macrophage-like phenotype

Our data demonstrated that systemic (IP) blockade of Notch2 induced a population of macrophages in the lung that was dependent on the recruitment of monocytes. To distinguish between the effects of Notch2 blockade in the periphery, e.g. on bone marrow hematopoiesis, and on cells in the lung, we administered antibodies directly into the airways by passive intratracheal inhalation (IT) at days 0 and 7, and assessed lung macrophages at day 14 using scRNAseq (Supplementary Fig. 1b). In control IT treated mice, we detected a moderate increase in the number of I4 macrophages, which likely reflects a response to the application of liquid to the lung. In contrast, IT treatment with αNotch2 antibody increased total numbers of IMs with the majority of cells expressing the same I4 marker genes (*Spp1, Gpnmb, Fabp5, Cd9*, and *Arg1*) (Fig. 4a–c, Supplementary Fig. 4a). AMs still shifted to the A2 phenotype, but there was no reduction in the numbers of patrolling monocytes (M2), and no change in the number of Esam-expressing

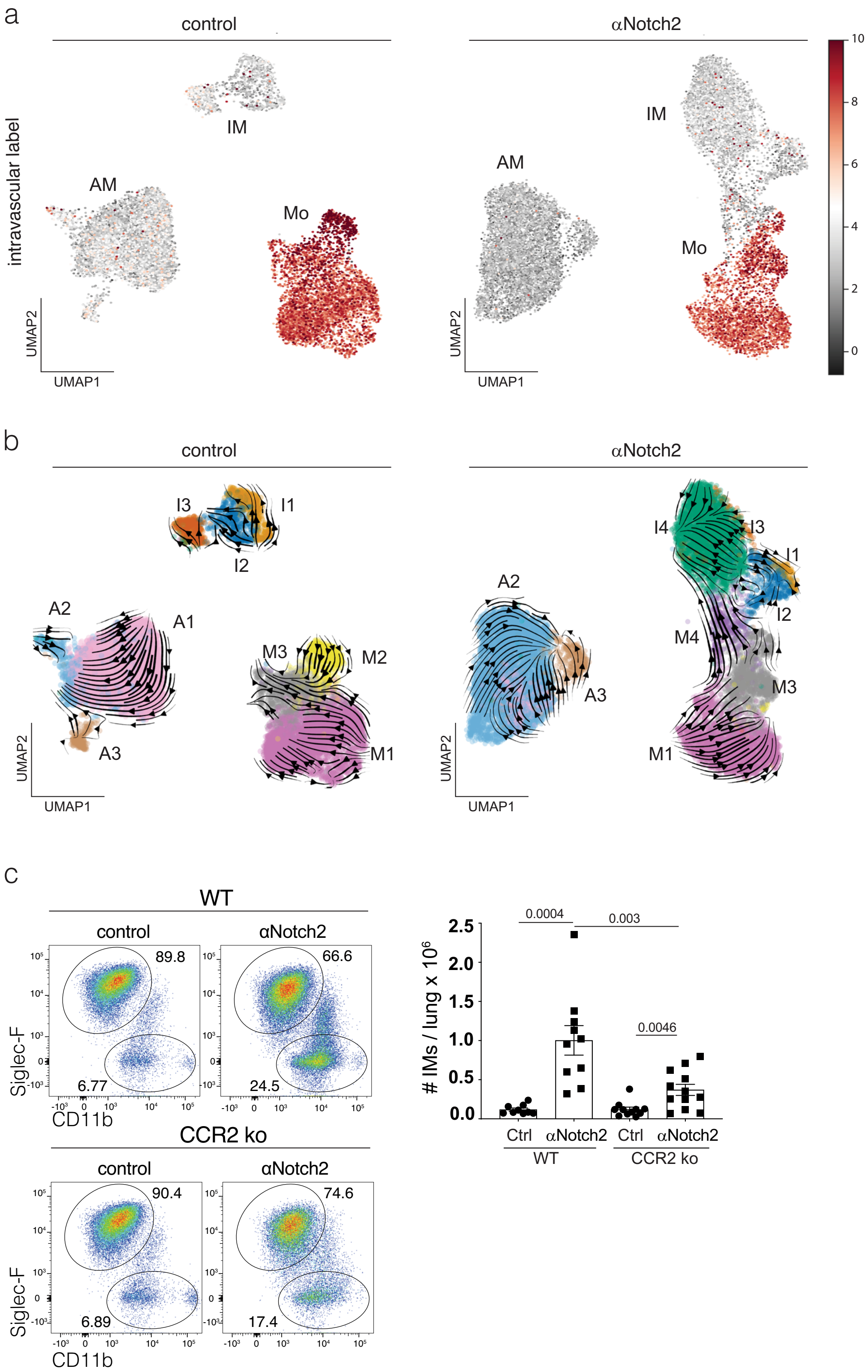

Fig. 3 | Cluster I4 macrophages are derived from monocytes. a Separate UMAP representation of cells from mice treated with control (left) or αNotch2 antibody (right). Intravascular CITE-Seq αCD45 antibody labels only monocytes in both conditions. After Notch2 blockade the lack of CITE-Seq intravascular αCD45 antibody staining of M4 monocytes (see b, and Supplementary Fig. 3) suggests that they have emigrated into tissue. **b** RNA-Velocity analysis of clustered cells after control (left) and αNotch2 (right) antibody treatment suggests that I4 macrophages derive from M4 monocytes. **c** Attenuation of IM expansion after Notch2 blockade in CCR2 KO mice. αNotch2 or control antibodies were administered to WT or CCR2 KO mice as shown in Supplementary Fig. 1b. Proportions of AMs compared to IMs determined by flow cytometry in WT and CCR2 KO mice are shown on the left. Absolute numbers of IMs are shown on the right. *n* = 9 WT-Ctrl, *n* = 10 WT-αNotch2, *n* = 11 CCR2ko-Ctrl, *n* = 12 CCR2ko-αNotch2. An unpaired parametric two-tailed t-test was applied for statistical analysis. Data is graphed as the mean +/- standard error of the mean (SEM).

cDC2s in the spleens[19] (Fig. 4b, Supplementary Fig. 4b), supporting that IT treatment largely restricted αNotch2 antibody to the lung.

We used a random forest classifier implemented in pySingleCellNet[36] with a calibrated output to classify and transfer the cell labels from the IP αNotch2 treatment to the IT dataset. Interestingly, a portion of the cells that clustered with I4 macrophages using a graph-based clustering algorithm were identified as A2 AMs by pySingleCellNet (Supplementary Fig. 4d). Accordingly, RNA velocity and pairwise cosine similarity between each of the clusters showed that I4 macrophages after local Notch2 blockade seemed to be transcriptionally more similar to AMs than to monocytes (Fig. 4d, e Supplementary Fig. 4c).

Identification of transcriptional states in I4 macrophages

To better understand the features that make up the I4 population, we analyzed the specific I4 transcriptional programs using Hotspot[37], a graph-based method that organizes genes into modules based on local autocorrelation and co-expression between nearby cells. To this end, both datasets (IT,IP) were integrated together as described before and Hotspot analysis was performed using the joint dataset of IT/IP Notch2 blockade (Fig. 5a–c, Supplementary Fig 5a). This allowed us to assess dynamic gene expression changes within a cluster and capture gradients of gene expression that would not naturally segregate into distinct subclusters.

Within cluster I4, Hotspot identified four gene modules: I4a, I4b, I4c, and I4d (Fig. 5a). Module I4a was defined by *Lgmn*, *Arg1, Fn1, Ccl9*, and alarmins *S100a6 and S100a4*. The I4a module was similarly expressed in I4 and M4 cells induced by systemic Notch2 blockade, but lowly expressed in A2. This indicated that expression of the I4a module is a signature for the monocytic origin of I4 cells after systemic antibody treatment (Fig. 5b, c; Supplementary Fig. 5b). Module I4b was marked by *Fabp5, Psap, Cd63, Gpnmb, Lgals3*, and *Spp1*, as well as many cathepsins (*Ctsd, Ctss, Ctsb, Ctsl*) (Fig. 5a). Most of these genes are known marker genes for 'lipid-associated' (LAM) or 'scar-associated' (SAM) macrophages[24,38]. This module was most highly and broadly expressed in I4 macrophages from both systemic and local Notch2 blockade and therefore describes the core I4 cell state (Fig. 5b, c; Supplementary Fig. 5b).

Module I4c was defined by the LAM/SAM and AM marker gene *Cd9*[24,38], as well as the AM marker genes *Atp6v0d2* and *Chil3* (Fig. 5a). It was expressed highest in A2 and I4 macrophages (Fig. 5b, c; Supplementary Fig. 5b). Finally, module I4d was defined by expression of AM marker genes *Ear2*, *Plet1*, *Wfdc21* and *Ltc4s* (Fig. 5a). The I4d signal was highest in AMs (A1-A3) but also present in I4 cells induced by IT but not by IP blockade (Fig. 5b, c; Supplementary Fig. 5b). Indeed, the more AM-specific module I4d was only expressed in 'AM-like' I4 macrophages which clustered closest to A2 AMs, further suggesting a potential relationship between AMs and I4 macrophages in IT but not IP treated mice (Fig. 5c, Supplementary Fig. 4d).

Resident AMs do not adopt an I4 macrophage state

To investigate whether these 'AM-like' I4 macrophages after IT Notch2 blockade derived from bona fide resident AMs, we transplanted congenically labeled AMs (CD45.2) into neonatal CD45.1$^+$ Csf2ra$^{-/-}$ mice that lack AMs due to the absence of GM-CSF signaling (henceforth, AM-transplant mice[39]). After 8-weeks, AM-transplant mice were administered control or αNotch2 antibody IT and analyzed as before (Fig. 5d). We differentiated between CD45.1$^+$ Csf2ra$^{-/-}$ host cells and transferred CD45.2$^+$ AMs using CD45.1 and CD45.2 Cite-Seq antibodies. As expected, AMs were labeled with CD45.2 antibodies, while IMs and monocytes were labeled with CD45.1 (Fig. 5d, e). Treatment with IT αNotch2 antibody induced I4 macrophages that were only expressing CD45.1, demonstrating that I4 macrophages induced by IT αNotch2 antibody did not derive from bona fide AMs (Fig. 5e). Furthermore, I4 macrophages clustered closer to monocytes and were more similar to transitional monocytes M4 than AMs (Supplementary Fig. 5c, d). We next applied the previously calculated Hotspot modules on the AM-transplant scRNA-Seq data (Supplementary Fig. 5e). Surprisingly, we found that after IT αNotch2 blockade in the AM-transplant model, the I4 cells lacked expression of AM cell module I4d (Fig. 5f; Supplementary Fig. 5e, f). Since monocytically derived AMs (MoAMs) cannot be generated in AM-transplant mice due to all monocytes lacking the GM-CSF receptor, monocytes recruited into the lungs of WT mice after IT Notch2 blockade likely acquire some AM-like features, potentially because of the environment in or around the alveolus. We did not detect significant numbers of I4 IMs in the alveolar space, suggesting that 'AM-like' I4 cells are located in the lung interstitium (Supplementary Fig. 5g).

Anti-Notch2 induced IMs resemble macrophage states in models of organ injury

The I4 macrophage gene signature is similar to a macrophage gene signature that has been previously described in injured organs and implicated in promoting fibrosis[24–27]. To determine how I4 macrophages compare to previously reported macrophages, we used our cell population labels and transferred the labels onto public scRNAseq studies using pySingleCellNet. A total of 12 public studies ranging from lung mouse models in the steady state (5 studies) to experimental models of organ insults (7 studies) were downloaded and processed similarly to our dataset before the label transfer procedure (Fig. 6, Supplementary Fig. 6).

Classification of steady-state IMs[9,12,15,16,40] as well as the respective no-treatment controls from the organ insult datasets showed that the vast majority of cells in these studies could be annotated as belonging to clusters I1, I2, and I3. A small percentage of cells could be classified as I4, suggesting that I4 macrophages are a bona fide but uncommon population in the steady state (Fig. 6a, b and Fig. 2b).

Public datasets of tissue insult came from seven different studies, largely focusing on different organs: liver[41], adipose tissue[38], skeletal muscle[42], heart[43], and three datasets from lung[27,44,45]. In epididymal fat pads and in livers of mice fed a high fat diet 0.7% and 15% of the macrophages were classified as I4 macrophages, respectively[38,41](Fig. 6b). In mouse models of organ injury, including infarcted heart, traumatic muscle injury, and several different models of lung fibrosis, between 15-70% of interstitial macrophages could be classified as I4 cells[27,42–45] (Fig. 6b). We compared the IMs from these studies with IMs from IP or IT αNotch2 treated by calculating a cosine similarity score after integrating all of the studies in the same PCA space (Supplementary Fig. 6a, b). IM cells associated with insult conditions showed high similarity to IMs after Notch2 blockade (Fig. 6c). Within the I4 population, I4 macrophages identified in mouse models of tissue insult were more similar to αNotch2-induced I4 cells than I4 cells identified in control mice (Supplementary Fig. 6c). Interestingly, a time-course study of bleomycin-induced lung fibrosis showed that there is a continuous expansion of cells resembling I4 macrophages until day 21 after bleomycin administration[45] (Fig. 6d).

We next evaluated the expression of the four I4 HotSpot gene expression modules in each of the published datasets. Scores were aggregated for each of the experimental conditions described in the respective study (Supplementary Table 1). In most studies, I4d (AM module) was prevalent in the controls (most likely identifying bona fide AMs in lung samples), while I4a, I4b, and I4c, were expressed at different levels depending on the study and condition (Supplementary Fig. 6d, e). Focusing on the bleomycin time course, we could identify a temporal expression pattern for each module where the I4a transcriptional state appeared first, with maximum signal at day 10, followed by an accumulation of I4b (Fig. 6e). This reflects the expression trajectories of modules in the systemic Notch2 blockade suggesting monocyte recruitment and conversion to I4 cells (Fig. 5). In this study, AM-enriched gene modules I4c and I4d were high at baseline, and were

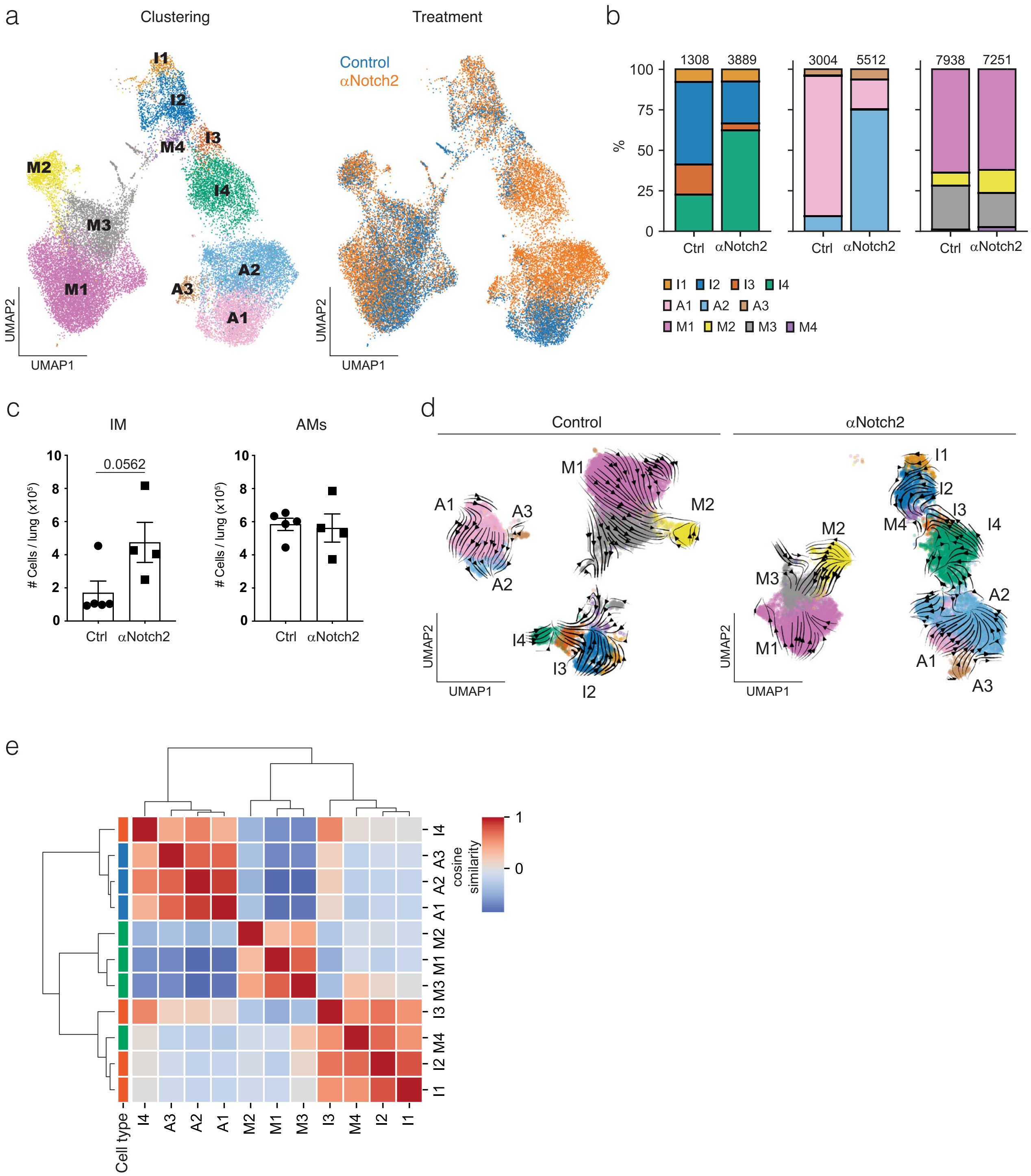

Fig. 4 | Intra-tracheal (IT) αNotch2 administration induces I4 macrophages that are similar to alveolar macrophages. IT Notch2 antibody treatment induces I4 macrophages. αNotch2 antibody ($n = 5$) or control antibody ($n = 5$) was given IT, in two doses, once a week for two weeks before the lungs were harvested. Myeloid cells were prepared for scRNAseq as described in Supplementary Fig. 2a, b. **a** scRNAseq analysis and unsupervised clustering of sorted AMs, IMs, and monocytes is shown as a UMAP. Colors represent cell clusters (left) or the treatment status of the mice (right). **b** Proportions of individual subclusters of IMs, AMs, and monocytes before and after treatment are shown in the bar graph. I4 IMs represent the majority of IMs seen after IT Notch2 blockade. The presence of M2 patrolling monocytes suggests that there is little systemic effect of IT administration. **c** Quantitation of IM numbers after IT Notch2 antibody blockade. Unpaired parametric two-tailed t-test was applied as statistical analysis. Data is graphed as the mean +/- SEM. **d** RNA-Velocity analysis suggests a potential connection between I4 macrophages and AMs. After control antibody treatment, AMs, IM, and monocytes are distributed separately (left Umap). After IT Notch2 blockade, I4 cells are positioned between AMs and IMs (right Umap). RNA-Velocity analysis shows potential transitions between AMs and I4 cells. Colors reflect unsupervised clustering identity (**a**). **e** Cosine similarity analysis of all AM, IM, and monocyte clusters in IT treatment showing a high similarity of cluster I4 to AMs.

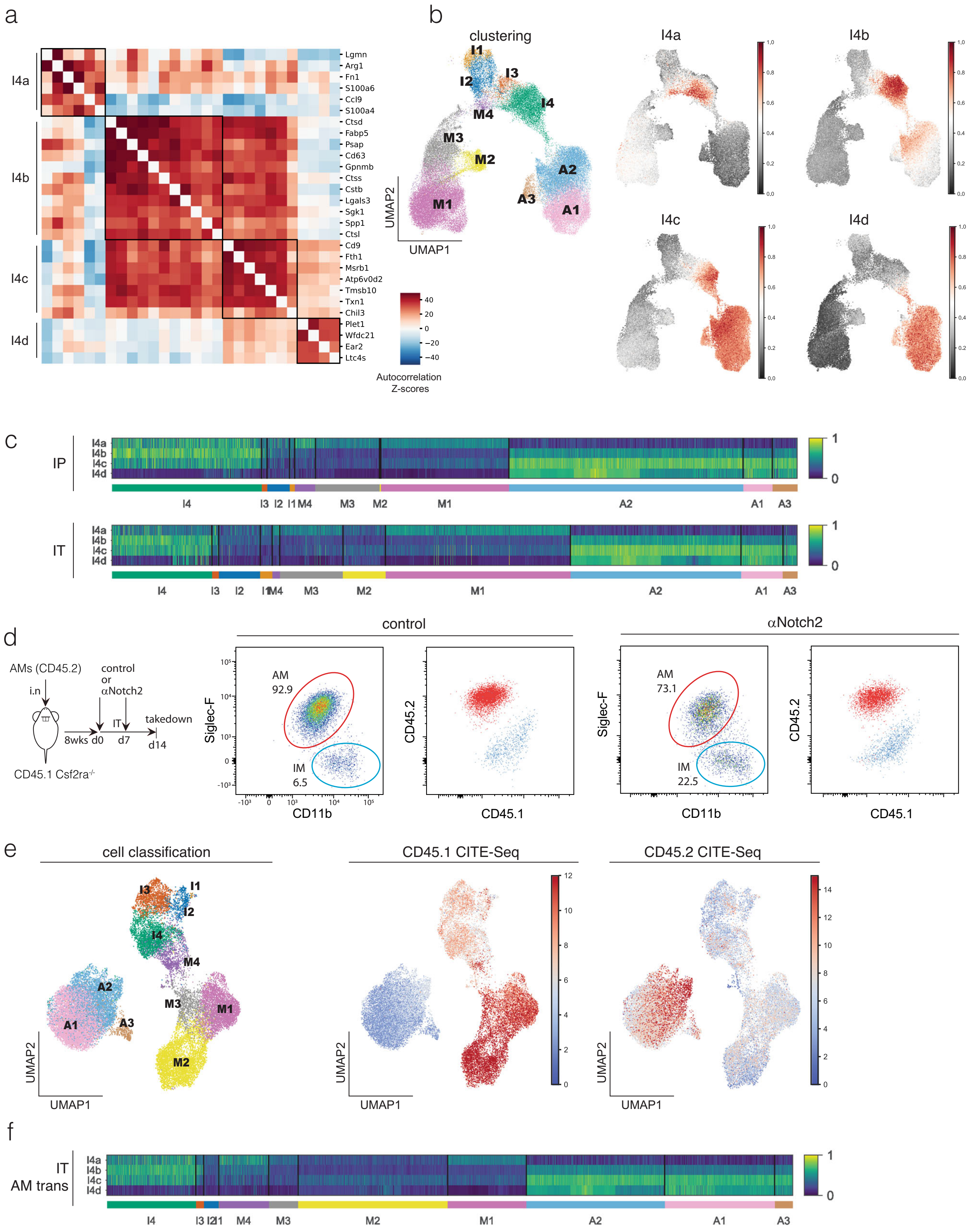

lost during acute inflammation before coming up again after day 10 suggesting the minimal contribution of AMs. This likely also reflects the initial loss of AMs during bleomycin-induced lung fibrosis[46] (Fig. 6e).

To determine whether Notch signaling might be modulated after injury, we used CellChatDB[47] to analyze Notch receptor – Notch ligand interactions in a whole lung dataset collected in control animals and after bleomycin injury[44]. This analysis showed that Notch - Notch-ligand interactions were reduced in the IM clusters after bleomycin (Fig. 6f). The loss of Notch interactions coincided with the appearance of I4 macrophages and supports the idea that loss of Notch signaling in vivo during tissue injury and inflammation may function as a signal to promote the I4 cell state.

Fig. 5 | Hotspot analysis identifies an I4 core gene module (I4b). Hotspot analysis of IP and IT IM subclusters identified 28 genes with significant pairwise local correlation that could be divided into four modules. **a** Heatmap showing the Z-scores for the local correlation values for the 28 genes in the four modules, I4a, I4b, I4c, and I4d. **b** Gene scoring for each of the modules projected on the joint IP/IT UMAP. Joint UMAP colored by cluster identification is shown on the left. The I4a module is expressed in cluster M4 and a subset of I4 cells. The I4b module is mainly expressed in cluster I4. Module I4c is expressed in cluster I4 and all AM subclusters. I4d is expressed primarily in AMs and in the AMs that bridge between cluster I4 and AMs. **c** Heatmap representation of I4a-d module expression in all monocyte, AM, and IM clusters, separated by the route of antibody application (IP - upper, IT - lower). **d** Schematic depiction of the experimental timeline (left) and flow cytometry analysis of AM-transplant model (right). CD45.2 AMs were transferred intranasally into CD45.1$^+$ Csf2ra$^{-/-}$ mice at neonatal state. Eight weeks later control or αNotch2 antibody was instilled IT as before. Mice were taken down 2 weeks after initial antibody instillation. Flow cytometry analysis confirms CD45.2 expression in AMs and CD45.1 expression in IMs. Cells from AM gate are shown in red in CD45.1/CD45.2 plot. Cells from IM gate are shown as blue in CD45.1/CD45.2 plot. Ungated cells from AM/IM gate are represented in gray. **e** scRNAseq analysis and unsupervised clustering of sorted AMs, IMs, and monocytes is shown as a UMAP. Colors represent cell clusters (left) or CITE-Seq antibody staining (right). CITE-Seq antibody counts were de-noised and scaled by background (dsb) and normalized counts were projected on scRNAseq UMAP. **f** Heatmap representation of I4a-d module expression in all monocyte, AM, and IM clusters in AM-transplant mice after IT αNotch2 antibody.

Testing the function of I4 macrophages in tissue injury

Since I4 macrophages are abundant in published datasets of lung injury and macrophages similar to the I4 phenotype are proposed to be drivers of tissue fibrosis[24,27,48,49], we tested whether their enrichment might modulate the fibrotic response after bleomycin-injury. We reasoned that if these macrophages are pro-fibrotic, expanding these macrophages before bleomycin injury should enhance the development of fibrosis. Mice were pretreated with αNotch2 antibody 10 and 3 days before bleomycin administration, timing the last bleomycin injection (day 4) so that it would be coincident with two weeks after the initial αNotch2 antibody treatment (Fig. 7a). Heavy water (D2O) was added to the drinking water to track new collagen deposition.

Body weight measurements showed that mice pre-treated with αNotch2 antibodies had significantly less weight loss over the course of the experiment (Fig. 7b). Histological examination of the lungs showed less inflammation and significantly less collagen deposition in the αNotch2 treated animals as indicated by H&E and trichrome staining, respectively (Fig. 7c, d). New collagen deposition based on isotope (deuterium) labeled hydroxyproline showed only a minimal increase of total and isotope labeled hydroxyproline in bleomycin-injured mice after Notch2 blockade (Fig. 7e). This demonstrates that macrophages with the I4 phenotype are not by themselves drivers of fibrosis and may play a role in attenuating fibrosis.

Bleomycin-induced injury increased IM numbers in lungs of control and αNotch2 treated animals 9 days after starting bleomycin applications, at the peak of inflammation (Supplementary Fig. 7a). To confirm that the macrophages that accumulate during bleomycin-induced injury after IP control or αNotch2 antibody treatment are similar to those that accumulate after Notch2 blockade without bleomycin, we performed scRNA-Seq on IMs from mice treated with αNotch2 alone or bleomycin +/- αNotch2. As expected, label transfer identified a population of cells similar to I4s after bleomycin treatment (Fig. 7f, Supplementary Fig. 7b). Cosine similarity calculations, based on the combined IM space with other injury datasets, demonstrated the similarity of macrophages seen after bleomycin treatment to macrophages from mice treated with αNotch2 antibody (Fig. 7g, Supplementary Fig. 6b). To verify that localized Notch2 blockade had the same protective effect, we administered bleomycin to mice pretreated IT with Notch2 antibodies. Similar to our results with systemic Notch2 blockade, mice treated with local Notch2 blockade showed less weight loss, less inflammation, and less fibrosis (Supplementary Fig. 7c, d). Importantly, Notch2 deletion in all non-hematopoietic cells using Rosa26$^{\mathrm{CreERT2}}$Notch2$^{\mathrm{flox/flox}}$ mice reconstituted with WT bone marrow, did not show protection against bleomycin-induced lung fibrosis, arguing that the beneficial effect of Notch2 blockade is due to its effect on the hematopoietic compartment in the lung and not on lung epithelial and/or stromal cells (Supplementary Fig. 7e).

To address the effect of Notch2 blockade in another, infectious, model of lung injury, we infected mice with a mouse-adapted strain of SARS-CoV-2 (MA-10)[50]. Mice were treated with αNotch2 or an isotype control antibody at 10 and 3 days before intranasal inoculation with SARS-CoV-2 MA-10. Animals were euthanized at days 2 and 7 for analysis of lung infection and injury. Notably, while viral RNA levels were equivalent in isotype and αNotch2-treated animals, less weight loss was observed in SARS-CoV-2 infected animals treated with αNotch2 antibody (Fig. 8a, b). Corresponding with the improved clinical outcome, much less airway space consolidation and immune cell infiltration was observed in αNotch2 compared to isotype antibody-treated mice (Fig. 8c). Overall these results show that blockade of Notch2-signaling attenuates inflammation in the lung after bleomycin-induced injury or viral infection, resulting in improved recovery.

Discussion

Over the last five years, there has been steady progress on the characterization of interstitial macrophages in the lung. Depending on the method used, previous studies using cell sorting, bulk RNA sequencing, and scRNA-Seq approaches have shown that there are two or three different interstitial macrophage populations in the lung[9,12,14,16]. Our work clearly supports the existence of three IM subtypes in the lung. Our approach combining cell sorting, scRNASeq, and CITE-Seq identified three distinct subtypes at high resolution which largely recapitulated populations described in previous studies. RNA velocity analysis of steady-state lungs did not show active monocyte to IM conversion, suggesting that these populations are relatively stable at steady state.

Given the role of Notch signaling controlling cell lineage identities, we were interested to study its role in regulating IM differentiation. We found that Notch2 signaling regulates monocyte-macrophage conversion in the lung. This was specific to Notch2 signaling, as Notch1 blockade had no effect on IMs. The increase of IM numbers in the lung after antibody mediated Notch2 blockade was intrinsic to the monocyte/macrophage axis as genetic deletion of Notch2 in mixed bone marrow chimeras phenocopied this effect. However, scRNA-Seq showed that Notch2 blockade induced cluster I4, a newly arising population of IMs, which strongly resembled macrophages previously described as lipid-associated macrophages (LAMs)[38] or scar-associated macrophages (SAM)[24]. RNA velocity analysis, experiments using CCR2ko mice, and lineage tracing experiments showed that these macrophages after systemic Notch2 blockade were mostly monocyte derived.

Systemic administration of blocking Notch2 antibodies could have widespread effects on cells outside and inside of the lung. To control for these effects we administered Notch2 antibodies locally by passive intratracheal inhalation (IT). The local confinement of the antibody was supported by the lack of changes in lung patrolling monocytes and in Notch2-dependent splenic ESAM2$^+$ cDC2s[19,22]. Upon IT instillation of αNotch2 antibody, I4 macrophages were still induced but some cells in the I4 macrophage cluster expressed genes that are specific to AMs, suggesting an AM origin. However, experiments where congenically marked WT AMs were transplanted into Csf2ra$^{-/-}$ mice that lack AMs, showed that I4 macrophages induced after IT Notch2 blockade were monocytically derived as no WT AMs adopted an I4 transcriptional phenotype. As this model does not allow for MoAM

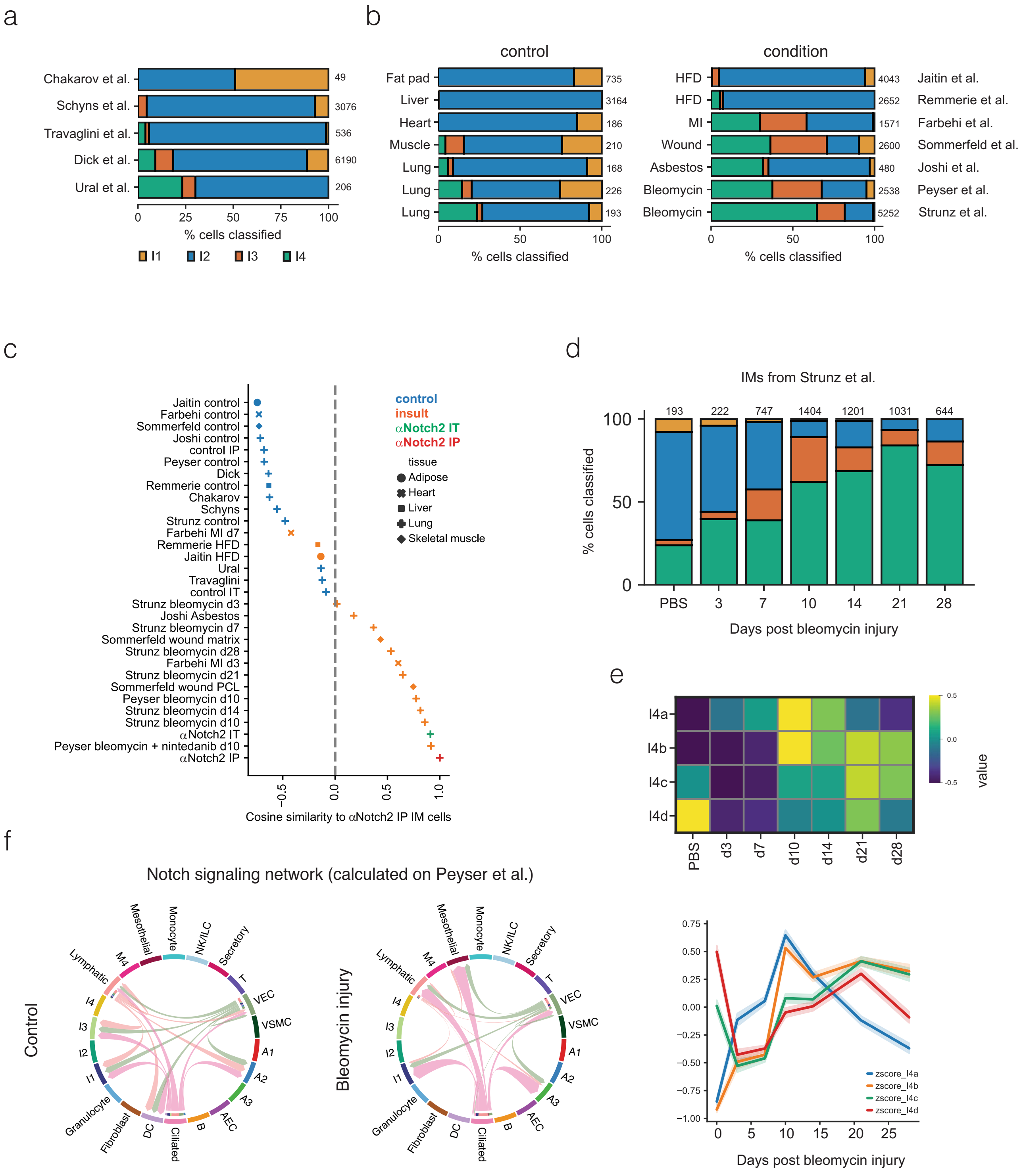

Fig. 6 | Comparison of macrophages generated in this study to macrophages in 12 previously published studies. a Cell classification of IMs from five published datasets[9,12,15,16,65] based on the clusters in our IP and IT datasets using pySingle-cellNet. Analysis of steady-state IMs identified in three IM subsets as well as a small fraction of I4 cells (green). Numbers on the right show the total number of analyzed cells in each study. **b** Analysis of IMs from insulted tissue from seven published studies as noted[27,38,41–45]. Label transfer using pySinglecellNet as in (**a**) identified variable numbers of I4 macrophages (green) with significant numbers in multiple lung injury studies. Control conditions are shown on the left and insulted conditions on the right. **c** Pairwise cosine similarity between aggregated IM cells from each study according to the experimental condition and compared to aggregated IMs after Notch2 antibody blockade. IMs after IP Notch2 application showed higher similarity to IM cells derived from insult conditions (in orange) and IT Notch2 antibody application (in green) than baseline or control samples across several tissues (in blue). **d** Proportion of cells classified as I4 increase in a lung bleomycin time-course study by Strunz et al.[45] **e** Hotspot module expression in all cells classified as AMs, IMs, or monocytes over a bleomycin lung injury time course from Strunz et al.[45] shows the progressive change in module expression over time. Data is presented as a heatmap (top) and xy-graph (bottom). **f** Decreased Notch receptor/ligand interactions detected in interstitial macrophages after bleomycin injury. CellChat analysis was performed from the whole lung scRNASeq data from Peyser et al.[44] focusing on Notch receptor-Notch ligand interactions.

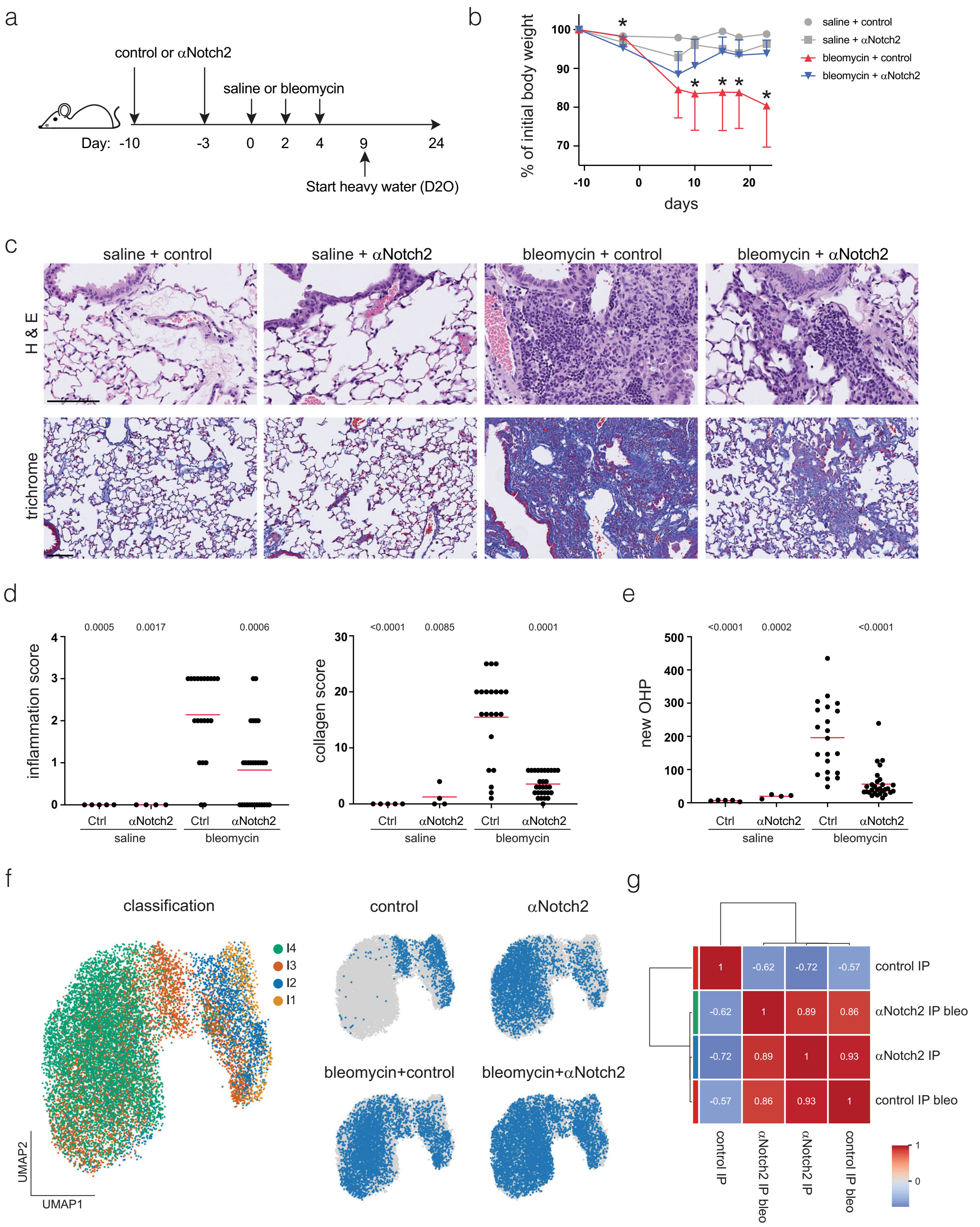

	control IP	αNotch2 IP bleo	αNotch2 IP	control IP bleo
control IP	1	-0.62	-0.72	-0.57
αNotch2 IP bleo	-0.62	1	0.89	0.86
αNotch2 IP	-0.72	0.89	1	0.93
control IP bleo	-0.57	0.86	0.93	1

development, this suggests that resident AMs, due to their long term imprinting in the alveolar space, have lost their plasticity to change as discussed by Guilliams and Svedberg[51]. It does not, however, rule out that I4 macrophages induced by IT Notch2 blockade could develop into MoAMs as I4 macrophages share some transcriptional similarities to ApoE^{+}CD11b^{+} AMs[52]. Interestingly, in AM-transplant mice, I4 macrophages lacked the expression of an AM specific gene module. This suggests that AM-specific genes induced by IT Notch2 blockade require the presence of GM-CSF, which they encounter when monocytes enter the alveolar interstitial space. Acquisition of the mature AM phenotype would likely occur after GM-CSF stimulated monocytes cross the alveolar wall into the alveolar space.

Fig. 7 | Notch2 antibody blockade ameliorates bleomycin induced lung fibrosis. **a** Schematic depiction of experimental timeline. **b** Mice pre-treated with αNotch2 antibodies exhibited decreased weight loss after bleomycin treatment. **c** Histological analysis shows that pre-treatment with αNotch2 antibodies ameliorates lung inflammation and fibrosis as assessed by H&E (upper panels) and trichrome (lower panels) staining. Scale bar = 100 µm. **d** Inflammation (left) and fibrosis (right) scoring. Sections were scored blindly using a scoring scale described in the Methods section. **e** Deuterated hydroxyproline levels (New OHP (ug/3 right lobes), mean + SD) were measured by mass spectroscopy (MS/MS) as an indicator of newly synthesized collagen. **f** Analyzed AMs, IMs, and monocytes were isolated from mice at day 9 according to the experimental layout depicted in (**a**). Integrated UMAP after Harmony batch correction of IM cells classified according to the cell populations defined in this study, colored by cluster identity (left), or colored in blue by experimental condition (right). **g** Pairwise cosine similarity of total aggregated IM space (Supplementary Fig. 6a, b) shows high similarity of total IMs in bleomycin-injured lungs and lungs treated with αNotch2 antibody. Mixed-effects model with Geisser-Greenhouse correction followed by a Tukey's multiple comparison test (**b**) or Kruskal Wallis test followed by Dunn's multiple comparison test vs. control antibody + bleomycin group. **b** For clarity only one asterisk is shown (*p = 0.0006 (day −3), 0.0068 (d10), 0.0001 (d15), 0.0002 (d18), <0.0001 (d23)) and only for the comparison of the control and αNotch2 groups in the bleomycin arm. Data are presented as mean values +/- SD. Each dot represents one mouse. Sample size **b**, **d**, **e**: Control antibody + saline (n = 5); αNotch2 + saline (n = 4); Control antibody + bleomycin (day 0: n = 30 (**b**), day 24: n = 21 (**d**, **e**)); αNotch2 + bleomycin (day 0: n = 30 (**b**), day 24: n = 29 (**d**, **e**)). One representative of two independent experiments.

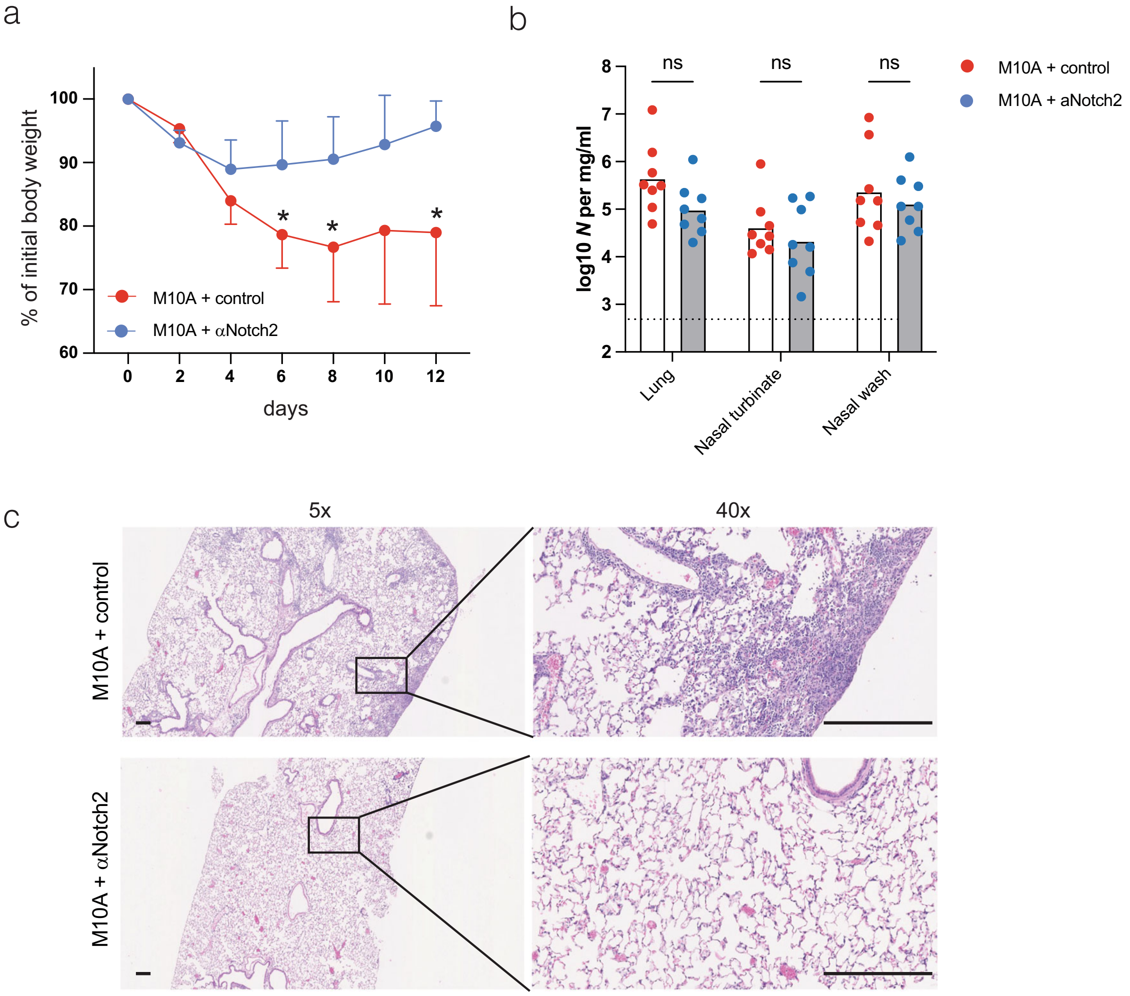

Fig. 8 | Notch2 antibody blockade ameliorated COVID-19 induced lung injury and fibrosis. **a** Mice pre-treated with control or αNotch2 antibodies were infected with the MA-10 mouse-adapted strain of COVID virus and were weighed every other day until mice were sacrificed on day 12. **b** Viral titers in mice treated with control or αNotch2 antibodies were measured by PCR. **c** Attenuation of inflammation in M10A infected animals after αNotch2 antibody treatment. H&E sections of lungs from mice pretreated with control or αNotch2 antibodies at 5X and 40X magnification. Scale bar = 100 µm. Mixed-effects model with Geisser-Greenhouse correction followed by Šidák's multiple comparison test (**a**); or unpaired parametric two-tailed t-test (**b**) were performed. **a** For clarity only one asterisk is shown (*p = 0.0022 (day 6), 0.0010 (d8), 0.0281 (d12)). Data are presented as mean values (**a**, **b**) +/- SD (**a**). Each dot represents one mouse. Sample sizes: **a** Control antibody + M10A infection (n = 15); αNotch2 + M10A infection (n = 11). **b** Control antibody + M10A infection (n = 8); αNotch2 + M10A infection (n = 8). Combined data from two independent experiments.

I4 macrophages have a gene signature similar to macrophages present in different models of organ injuries. Examples of these macrophages are lipid-associated macrophages (LAMs)[24,38], 'scar-associated macrophages' (SAMacs)[24,38] which localize in areas of excessive extracellular matrix deposition[24,48], and macrophages in livers of mouse models of NASH[41,53]. In humans, macrophages expressing these genes are reported to be present in patients with liver cirrhosis and in lung fibrosis[24,48,49]. While our analysis of a published whole lung scRNA-Seq dataset supports the idea that Notch signaling is downregulated during tissue injury, the limited availability of whole tissue datasets before and after injury prevented us from confirming this hypothesis more widely.

To study the similarity of I4 macrophages from Notch2 blockade to macrophages seen in various other studies[27,42–45], we used random forest models to identify and label potential I4 cells in published studies and then overlaid our HotSpot modules. Our analysis suggests that the I4 macrophage signature from both IP and IT αNotch2-treated mice is very similar and also similar to damage-associated macrophages reported in other studies. The HotSpot analysis suggests that I4 macrophages share a common geneset (I4b) and that differences among different I4 macrophages in different tissues and injuries reflect environmental and developmental cues.

A previous study showed that macrophages labeled as I4 macrophages begin to accumulate in the lung about 3 days after bleomycin injury and represent the majority of interstitial macrophages during the fibrotic phase (day 14-20)[45]. Their presence in many fibrotic conditions suggested their potential roles in promoting fibrosis after tissue injury[24–27], while others suggested that macrophages with a similar gene signature could help attenuate liver fibrosis or aid in bacterial defense in the lung[52,53]. In our studies, the accumulation of I4 macrophages prior to bleomycin-induced injury clearly did not promote fibrosis and may have attenuated it. This argues that macrophages with this phenotype are not per se drivers of lung fibrosis. We cannot rule out, however, that the presence of these cells after the initiation of a fibrotic process could contribute to the pathogenesis. Additionally, despite the strong calculated similarity between αNotch2-induced I4 macrophages and injury-induced I4 macrophages and the shared HotSpot (I4b) module, we cannot exclude that other differences in the gene expression are functionally important.

Notch signaling is ubiquitous and antibody blockade has effects on cells other than monocytes inside and outside of the lung. IT administration of αNotch2 antibodies largely limited exposure to the lung as it had no effect on the number of patrolling monocytes or splenic ESAM$^+$cDC2s but still conferred the same protection against bleomycin-induced fibrosis. Importantly, using bone-marrow chimeras, deleting Notch2 on the non-hematopoietic compartment did not have an effect on the progression of bleomycin-induced lung fibrosis suggesting that the protection seen after Notch2 blockade is mediated by the hematopoietic compartment in the lung.

The rapid adoption of single cell transcriptomic approaches over the last several years has provided insights into the pathogenesis of disease by revealing novel cell states as in the case of macrophages that are present during maladaptive tissue responses. It is tempting to implicate such cell states with progression of the pathological response, but such cell states may be a bystander response or even an insufficient protective response. Our results demonstrate that the I4 macrophages seen in many models of organ injury and human diseases are not pro-fibrotic per se and may even be protective. More precise genetic tools and approaches will be required to dissect the role of individual cell states in disease.

Methods

Mice

Animals were maintained in accordance with the Guide for the Care and Use of Laboratory Animals (National Research Council 2011, Guide for the Care and Use of Laboratory Animals: Eighth Edition. Washington, DC: The National Academies Press. https://doi.org/10.17226/12910.). Genentech is an AAALAC-accredited facility and all animal activities in this research study were conducted under protocols approved by the Genentech Institutional Animal Care and Use Committee (IACUC).

Mice were housed in individually ventilated cages within animal rooms maintained on a 14:10-hour, light:dark cycle. Animal rooms were temperature and humidity-controlled, between 68 to 79 °F (20.0 to 26.1 °C) and 30 to 70% respectively, with 10 to 15 room air exchanges per hour. Mice were fed an autoclaved, closed formula, natural ingredient diet ad libitum (Laboratory Autoclavable Rodent Diet 5010, Lab Diet, Richmond, IN) and provided reverse osmosis purified drinking water ad libitum.

Mice were bred and maintained in groups of 1–5 animals per cage at Genentech. Males and females from 6–20 weeks old were used. Mice were euthanized using CO_2.

Wild type C57BL/6 J mice were obtained from Jackson Laboratory and used directly throughout the study. Other strains were obtained from various sources and bred in house: CD45.1 congenic mice (Jackson Laboratory B6.SJL-Ptprca Pepcb/BoyJ, Strain #002014); Notch2$^{f/f}$ (Jackson Laboratory B6.129S-Notch2tm3Grid/J, Strain #010525); ROSA-Cre^{ERT2} (University of Tokyo); CCR2ko (The J. David Gladstone Institute).

Notch2$^{f/f}$ mice containing *loxP* sites flanking Exon3 of the Notch2 locus were crossed with ROSA-Cre^{ERT2} to obtain conditional deletion of Notch2 in cells expressing both alleles. CD45.1 mice were bred in house with C57BL/6 mice to obtain CD45.1 + 2 congenic mice to use in chimera studies.

Csf2ra KO mice (pmid: 27468760) were crossed to C57BL/6 congenic CD45.1 (strain 002014) and housed at the University of Zurich Laboratory Animal Sciences Center in Zurich, Switzerland, in a specific pathogen-free barrier facility in individually ventilated cage units. Animal experiments were reviewed and approved by the cantonal veterinary office of Zurich (ZH111/2022).

Antibodies

A list of used commercially available analysis antibodies can be found in Supplementary Table 2.

Anti-notch antibody treatments

Anti-Notch1 and anti-Notch2 antibodies have been previously described[28]. Anti-Notch receptor antibodies were injected at 20 mg/kg of mouse in PBS medium, once per week for two weeks, unless a different timeline is specified. Intratracheal antibody was applied at 15 mg/kg using passive intratracheal inhalation as described below.

Tamoxifen treatments

Tamoxifen (MP Biomedicals, LLC) was dissolved in sunflower seed oil and administered at 80 mg/kg once a day for 5 consecutive days. Mice were analyzed 10 days after the last tamoxifen injection for quantification of macrophage populations. For bleomycin injury experiments, mice were instilled with bleomycin at days 10, 12, and 14 after the last tamoxifen injection.

Bone marrow chimeras

Donor bone marrow was isolated from femur and tibia by crushing with mortar and pestle, and removing debris by filtering through a 70um filter. Red blood cells were removed using ACK lysing buffer (Gibco) and cells were resuspended at 10×10^6 cells per ml. Recipient mice were irradiated twice a day at 550 rad and 2×10^6 cells from donor bone marrow was administered intravenously after the second irradiation in a volume of 200ul. Bone marrow chimeric mice were rested for a minimum of 12 weeks before undergoing tamoxifen injections.

Isolation and Intranasal Transplantation of Alveolar Macrophages

CD45.2$^+$ WT AMs were harvested from donor mice by BAL: Mice were euthanized by lethal i.p. pentobarbital injection. The trachea was exposed and cannulated with a 20-G catheter.

1 mL of warm PBS supplemented with 2 mM EDTA was instilled intratracheally and incubated for 5 min. Without removing the catheter or syringe, the lung was flushed three times with ~0.7 mL of the installed EDTA-containing PBS, and the BAL fluid was then collected into cold PBS supplemented with 2% FCS. Instillation and flushing were repeated three more times with 1 mL PBS supplemented with 2 mM

EDTA without the 5 min incubation period. Collected BAL fluid was then centrifuged at 300 *g* for 5 min at 4 °C. Cells were then counted with trypan blue staining using Neubauer chamber. For the intranasal transplantation of CD45.2$^+$ WT AMs, neonatal CD45.1$^+$ *Csf2ra*$^{-/-}$ mice (postnatal day 0) were anesthetized with isoflurane and transplanted with 1 ×10^5 CD45.2$^+$ WT AMs resuspended in PBS and in a total volume of 10 uL.

Tissue processing

Lung lobes were collected making sure to separate them from the trachea and lymph nodes. Lungs, kidney, heart, and spleen were minced and then digested in 1-5 ml of complete RPMI containing 25ug/ml of liberase (Roche) and 0.1 mg/ml of DNAseI (Roche) in an incubator at 37°C for 30 minutes with gentle shaking. Samples were then mashed through 70um filters, centrifuged and red blood cells were lysed using ACK buffer (Gibco). Cell numbers were counted using Vicel cell counter, and aliquots from each sample were stained with antibodies for flow cytometry. Peritoneal macrophages: Peritoneal lavage was performed on deceased mice using 10 mL of PBS or 5 mL 2 mM EDTA + 2% BSA in PBS. They were then centrifuged and stained with antibodies for flow cytometry. Liver macrophages: Livers were digested using Liver Dissociation kit (Miltenyi) using C-tubes with gentleMACS Octo Dissociator with Heaters. After digestion, C-tubes were spun down and the supernatant was removed. Liver cells were resuspended in 33% Percoll (Sigma), transferred to 15 ml eppendorf tubes and centrifuged at 1100 x *g* at room temperature for 20 minutes without break. Supernatants were carefully removed and pellet containing immune cells were collected. Red blood cells were lysed using ACK buffer (Gibco). Cell numbers were counted using Vi-CELL XR cell counter (Beckman Coulter), and aliquots from each sample were stained with antibodies for flow cytometry, data was acquired using a BD Symphony A3/A5.

5 lasers (355 nm, 405 nm, 488 nm, 561 nm, 638 nm; Software: BD FACSDiva Software v9.0) and analyzed in FlowJo (FlowJo 10.10.0).

Histology

The lung was removed and flushed with 10% neutral buffered formalin to inflate the tissue. A suture was then tied to the trachea to ensure the tissue stayed inflated while fixing in 10% neutral buffered formalin for 24 h. After fixation, the samples were transferred to 70% ethanol and then processed for paraffin embedding. Once embedded, the blocks were trimmed on a Leica RM-2245 microtome until the center of the tissue was reached. Five-micrometer-thick sections were stained with hematoxylin and eosin (H&E) and Masson's trichrome, and a single section from each animal was qualitatively scored for inflammation and fibrosis severity. Pulmonary inflammation was scored on H&E stained sections according to the following criteria: 0, normal lung; 1, minimal inflammation (infrequent/sparse inflammatory infiltrates); 2, mild inflammation (light perivenous involvement); 3, moderate inflammation (many small foci of mononuclear cells); 4, Severe inflammation (generalized mononuclear infiltrates). Trichrome-stained sections were scored for the number and size of fibrotic foci and a fibrosis score was obtained by multiplying the two scores. Number of foci (A): 0, none detected; 1, <25% tissue section; 2, 25-50% tissue section; 3, multiple discrete foci across >50% section; 4, multifocally coalescent or locally extensive fibrosis; 5, diffuse fibrosis. Size of foci (B): 0, none detected; 1, largest focus <area of ~2 alveolar spaces; 2, largest focus <area of ~4 alveolar spaces; 3, coalescing areas >4 alveolar spaces; 4, locally extensive fibrosis; 5, diffuse fibrosis. Fibrosis score = number of foci (A) x size of foci (B).

For SARS-CoV-2 infection studies, the lungs (right lobe) of euthanized mice were inflated with 1 to 2 mL of 10% neutral buffered formalin using a 3-ml syringe after a catheter was inserted into the trachea. Lungs were then kept in fixative for 7 days. Tissues were embedded in paraffin, and sections were stained with hematoxylin and eosin. Images were captured using the Nanozoomer (Hamamatsu) at the Alafi Neuroimaging Core at Washington University.

Bleomycin administration, deuterated water labeling, and hydroxyproline measurement

Adult mice (older than 12 weeks) were randomized based on their weights before the study to minimize variance between experimental and control groups. Bleomycin was administered via passive intratracheal inhalation dosing on days 0, 2, and 4 at 0.24 U/kg (DNC 0703–3155-01; TEVA).

For passive intratracheal inhalation 53ul of bleomycin or antibody dosing solution was delivered to a soft pipette tip (gel loading tip) and the tip was inserted into the airway, visibly locating the opening of the trachea in the open mouth. When the pipette tip created a seal in the airway, the dosing solution was inhaled into the lung. After delivery, animals were monitored continuously on a 37°C heat pad until fully awake and ambulatory.

Deuterated water labeling was used to assess the new collagen synthesis in bleomycin studies[54]. Deuterium labeling started on day 9 after bleomycin delivery[55], by injecting deuterated water i.p. (DLM-4-99.8-1000; Cambridge Isotope Laboratories) 35 mL/kg in 2 divided doses 4 hours apart. Afterward, 8% deuterated water in drinking water was provided ad lib in a water bottle until the end of the study.

Deuterated water incorporation into hydroxyproline was analyzed as described previously[56].

Mass spectrometry and analysis were performed by Metabolic Solutions. New hydroxyproline content was expressed as µg per 3 right lung lobes.

MA-10 virus infection experiments and measurement of viral burden

The MA-10 strain of SARS-CoV-2 has been described previously[50]. Virus was passaged once in Vero-TMPRSS2 cells and subjected to next-generation sequencing to confirm the identity of the virus and stability of the amino acid substitutions. All virus experiments were performed in approved biosafety level 3 (BSL−3) facilities. Viral infection experiments were performed at Washington University School of Medicine. Animal studies were carried out in accordance with the recommendations in the Guide for the Care and Use of Laboratory Animals of the National Institutes of Health. The protocols were approved by the Institutional Animal. Care and Use Committee at the Washington University School of Medicine (assurance number A3381−01). Virus inoculations were performed under anesthesia that was induced and maintained with ketamine hydrochloride and xylazine, and all efforts were made to minimize animal suffering. Sample size for animal experiments was determined on the basis of criteria set by the institutional Animal Care and Use Committee. Experiments were neither randomized nor blinded.

Cohorts of 22-week-old male C57BL/6 mice were administered αNotch2 or isotype control antibodies (20 mg/kg) at days 10 and 3 before inoculations with 10^5 FFU of SARS-CoV-2 MA-10. Weights were recorded daily. Animals were euthanized at 7 dpi, and nasal wash, nasal turbinates, and left lungs were harvested for virological analyses. Right lung lobes were collected for pathological analyses.

For the measurement of viral burden, tissues were weighed and homogenized with zirconia beads in aMagNA Lyser instrument (Roche Life Science) in 1 mL of DMEM medium supplemented with 5%heat-inactivated FBS. Tissue homogenates were clarified by centrifugation at 10,000 rpm for 5 min and stored at −80 °C. RNA was extracted using the MagMax mirVana. Total RNA isolation kit (Thermo Fisher Scientific, A27828) on the Kingfisher Flex extraction robot (Thermo Fisher Scientific). RNA was reverse transcribed and amplified using the TaqMan RNA-to-CT 1-Step Kit (ThermoFisher Scientific). Reverse transcription was carried out at 48 °C for 15 min followed by 10 min at 95 °C. Amplification was accomplished over 50 cycles as follows: 95 °C for 15 s and 60 °C for 1 min. Copies of SARS-CoV-2 N gene RNA in samples were determined by RT-qPCR cycle threshold (Ct) values which were then converted to transcript or genome copy number equivalents by generating an RNA standard curve[57].

Single cell library preparation and sequencing

scRNA sequencing was performed using Chromium Next GEM Single Cell 5′ Kit v2 protocol following the manufacturer's instructions (10X Genomics, Cat. PN-1000263). Lung tissue from mice of specific treatments was processed as described in the "Tissue Processing" section. Dissociated cells were then stained with flow cytometry antibodies (for sorting by flow cytometry), Cite-seq antibodies (for protein expression of cell-specific markers, Biolegend) and barcode hashtag antibodies (for differentiation of each replicate mouse, Biolegend) (Supplementary Fig. 2b). Stained cells were pooled by treatment, and FACS-sorted for AM, IM, and monocytes using a BD FACSAria Fusion or BD FACSSymphony S6 (5 lasers: 355 nm, 405 nm, 488 nm, 561 nm, 638 nm; 100 μm nozzle @ 20 psi @ ~30 kHz; Sorting precision mode:4-Way Purity; Software: BD FACSDiva Software v9). An approximately equal number of cells from each treatment were pooled by cell type, counted, and checked for viability using Vi-CELL XR cell counter (Beckman Coulter) or hemocytometer. Finally, cells were injected into microfluidic chips to form Gel Beads-in-Emulsion (GEMs) in the 10X Chromium instrument. AM, IM, and monocytes were injected into separate lanes. Reverse transcription (RT) was performed on the GEMs, and RT products were purified and amplified. DNA from antibody-derived tags (ADTs) was separated from cDNA based on size selection using SPRIselect beads (Beckman Coulter, cat. B23318) and cDNA was used to generate Gene expression libraries. ADT/HTO libraries were generated using 5′ Feature Barcode Kit, (10Xgenomics PN-1000256). Gene expression and ADT/HTO libraries were then profiled using the Bioanalyzer High Sensitivity DNA kit (Agilent Technologies, cat. 5067-4626) and quantified with Kapa Library Quantification Kit (Roche, cat. 07960255001). Illumina HiSeq and NovaSeq (Illumina) were used to sequence the libraries.

Analytical methods

Initial data processing of single cell barcode libraries. Alignment of HTO and CITE-seq libraries was performed using the CellRanger workflow as implemented in Cumulus[58] against TotalSeq-C and specific antibody sequences (Supplementary Fig. 2b) using the "fiveprime" chemistry setting. Feature barcode demultiplexing was performed using the demultiplexing workflow implemented in Cumulus which uses DemuxEM[59]; and normalization of CITE-seq protein counts using the denoised and scaled by background method[60] as implemented in the python library muon[61].

Initial data processing and quality control of single cell RNA-seq. Initial processing of scRNA-seq libraries generated in this study was performed using the STARSolo workflow as implemented in Cumulus[58] (version 2.4.1). Gene expression reads were aligned against the mm10 reference genome, with the assay option "tenX_5p" to indicate 10×5′ assay, and "Gene Velocyto" in the SoloFeatures to obtain total gene counts as well as spliced, unspliced, and ambiguous counts per cell per gene. Cell by gene matrices for public datasets were downloaded already as raw counts, obtained as described in the respective study.

To remove doublets and poor-quality cells, cells were excluded from the analysis if they were outliers in the corresponding dataset in terms of number of genes, number of unique molecular identifiers (UMIs) and percent of mitochondrial genes. In addition, when hashing information was available, cells were further removed if more than one HTO was assigned by DemuxEM.

Normalization, batch correction, clustering and visualization. The computational analysis for the filtered and quality-controlled cells was largely performed using the python package Scanpy[62] using standard protocols. Briefly, cell-by-gene count matrices were total-count normalized to 10,000 reads per cell. Counts were further logarithmized before selecting highly variable genes with a mean expression between 0.01 and 5, and a mean dispersion of 0.5. Selected genes were used to compute a principal components analysis, and visualized by computing a UMAP using the top 30 principal components. The neighborhood graph was also computed using the PCA representation of the data matrix, and used to calculate clusters using the leiden algorithm. When indicated, Harmony[63] was used to integrate datasets by study, and this new projection used to recalculate the neighborhood graph and UMAP embedding.

Identification of myeloid cells. Cell-by-gene normalized counts were used as input for cell annotation using the package SingleR[31] and the Immgen database. The identity of each cell was assigned according to the label with the maximum score value. To annotate cell populations, cells were clustered at low resolution and assigned a cell type identity by taking the label with the highest average in the cluster. Only cells assigned a macrophage or monocyte label were taken for further analysis.

Label transfer of annotations in this study. The cell-by-gene raw counts matrix for both IP and IT datasets with the cluster annotations was used as training dataset for label classification using the python implementation of SingleCellNet[36]. The original code was modified to produce a calibrated probability with isotonic regression using the library scikit-learn. For each dataset to be queried, the cell-by-gene raw counts matrix as published in the original study was filtered to include only the common genes with the training dataset. The cell identity assigned corresponds to the label with the maximum calibrated probability, or to a random category, created by randomizing the training dataset. Cells were further added to the random category if the calibrated probability was below 0.7.

Calculation of RNA velocity vectors. Cell by gene total, unspliced and spliced raw counts were used as input for RNA velocity analysis using the python library scvelo[64], and processed as indicated in the library documentation. Briefly, genes with less than 20 counts in both unspliced and spliced matrices were excluded from the analysis. Further, the first and second order moments (means and uncentered variances) were computed among the 30 nearest neighbors using the top 30 principal components, and the dynamical model was applied to learn the transcriptional dynamics of splicing kinetics. Velocity pseudotime was calculated using scvelo velocity_pseudotime function.

Identification of transcriptional modules using HotSpot. IP and IT myeloid datasets after IP αNotch2 treatment were integrated using Harmony, and the raw counts from IM cells used as input to identify gene modules with local correlation in the batch corrected space using HotSpot[65]. Gene expression was modeled using the depth-adjusted negative binomial as background, and total UMI counts as per-cell scaling factor. Only the top 1000 genes with an autocorrelation with an FDR < 0.5 were selected to compute pairwise local correlations. Modules were further created using a minimum threshold of 20 genes. To identify significant modules enriched in I4 macrophages each module was scored against all myeloid cells using the scoring function provided by HotSpot and only modules with specific expression in I4 cells were selected. Within those modules, genes were filtered out if the autocorrelation coefficients were below 0.3, and the Z-score for autocorrelation was below 130.

Cosine similarity. Cell-to-cell similarity was quantified in either PCA or Harmony corrected PCA space using the cosine similarity implementation by scikit-learn, and the mean of the space as center.

Inference of cell-cell communication using CellChat. The whole lung scRNA-seq dataset from Peyser et al.[44] was processed, filtered, annotated, and annotated with SingleR to obtain general cell type annotations, and with our cluster labels with SingleCellNet to classify IM populations as previously described. Normalized counts were used as input to run CellChat using the cluster annotation as cell group information and subsetting specifically for the Notch pathway.

Library versions used: scanpy 1.9.5, anndata 0.9.2, scvelo 0.3.2, hotspot 1.1.1, scipy 1.10.1, matplotlib 3.7.3, pySingleCellNet 0.1.

Reporting summary

Further information on research design is available in the Nature Portfolio Reporting Summary linked to this article.

Data availability

The scRNAseq and barcode data generated in this study have been deposited in the GEO database under accession code GSE243289 and accession code GSE277297. Previously published scRNAseq datasets of steady state lung macrophages can be found under accession numbers GSE188647[9] [https://www.ncbi.nlm.nih.gov/geo/query/acc.cgi?acc=GSE188647], GSE125691[12] [https://www.ncbi.nlm.nih.gov/geo/query/acc.cgi?acc=GSE125691], GSE146683[15] [https://www.ncbi.nlm.nih.gov/geo/query/acc.cgi?acc=GSE146683], E-MTAB-7678[16] [https://www.ebi.ac.uk/biostudies/arrayexpress/studies/E-MTAB-7678], and PRJNA632939[65] [https://www.ncbi.nlm.nih.gov/sra/?term=PRJNA632939]. Previously published scRNAseq datasets from different models of organ insult can be found under accession numbers GSE127803[27] [https://www.ncbi.nlm.nih.gov/geo/query/acc.cgi?acc=GSE127803], GSE128518[38] [https://www.ncbi.nlm.nih.gov/geo/query/acc.cgi?acc=GSE128518], GSE156059[41] [https://www.ncbi.nlm.nih.gov/geo/query/acc.cgi?acc=GSE156059], GSE138027[42] [https://www.ncbi.nlm.nih.gov/geo/query/acc.cgi?acc=GSE138027], E-MTAB-7376[43] [https://www.ebi.ac.uk/biostudies/arrayexpress/studies/E-MTAB-7376], GSE129605[44] [https://www.ncbi.nlm.nih.gov/geo/query/acc.cgi?acc=GSE129605], and GSE141259[45] [https://www.ncbi.nlm.nih.gov/geo/query/acc.cgi?acc=GSE141259]. All other data are available in the article and its Supplementary files or from the corresponding author upon request. Source data are provided with this paper.

Code availability

Code to reproduce the analyses described in this manuscript can be accessed via: https://github.com/Genentech/2024_cruz_etal.

References

1. Davies, L. C., Jenkins, S. J., Allen, J. E. & Taylor, P. R. Tissue-resident macrophages. *Nat. Immunol.* **14**, 986–995 (2013).
2. Guilliams, M., Thierry, G. R., Bonnardel, J. & Bajénoff, M. Establishment and maintenance of the macrophage niche. *Immunity* **52**, 434–451 (2020).
3. Alliot, F., Godin, I. & Pessac, B. Microglia derive from progenitors, originating from the yolk sac, and which proliferate in the brain. *Dev. Brain Res.* **117**, 145–152 (1999).
4. Ginhoux, F. et al. Fate mapping analysis reveals that adult microglia derive from primitive macrophages. *Science* **330**, 841–845 (2010).
5. Schulz, C. et al. A lineage of myeloid *Cells* independent of Myb and hematopoietic stem cells. *Science* **336**, 86–90 (2012).
6. Yona, S. et al. Fate mapping reveals origins and dynamics of monocytes and tissue macrophages under homeostasis. *Immunity* **38**, 79–91 (2013).
7. Guilliams, M. et al. Alveolar macrophages develop from fetal monocytes that differentiate into long-lived cells in the first week of life via GM-CSF. *J. Exp. Med.* **210**, 1977–1992 (2013).
8. Park, M. D., Silvin, A., Ginhoux, F. & Merad, M. Macrophages in health and disease. *Cell* **185**, 4259–4279 (2022).
9. Dick, S. A. et al. Three tissue resident macrophage subsets coexist across organs with conserved origins and life cycles. *Sci. Immunol.* **7**, eabf7777 (2022).
10. Kawano, Y. et al. Colonic pro-inflammatory macrophages cause insulin resistance in an intestinal ccl2/ccr2-dependent manner. *Cell Metab.* **24**, 295–310 (2016).
11. Sabatel, C. et al. Exposure to bacterial CpG DNA protects from airway allergic inflammation by expanding regulatory lung interstitial macrophages. *Immunity* **46**, 457–473 (2017).
12. Chakarov, S. et al. Two distinct interstitial macrophage populations coexist across tissues in specific subtissular niches. Science **363**, eaau0964 (2019).
13. Zaman, R. et al. Selective loss of resident macrophage-derived insulin-like growth factor-1 abolishes adaptive cardiac growth to stress. *Immunity* **54**, 2057–2071.e6 (2021).
14. Gibbings, S. L. et al. Three unique interstitial macrophages in the murine lung at steady state. *Am. J. Resp. Cell Mol.* **57**, 66–76 (2017).
15. Ural, B. B. et al. Identification of a nerve-associated, lung-resident interstitial macrophage subset with distinct localization and immunoregulatory properties. *Sci. Immunol.* **5**, eaax8756 (2020).
16. Schyns, J. et al. Non-classical tissue monocytes and two functionally distinct populations of interstitial macrophages populate the mouse lung. *Nat. Commun.* **10**, 1–16 (2019).
17. Lewis, K. L. et al. Notch2 receptor signaling controls functional differentiation of dendritic cells in the spleen and intestine. *Immunity* **35**, 780–791 (2011).
18. Caton, M. L., Smith-Raska, M. R. & Reizis, B. Notch–RBP-J signaling controls the homeostasis of CD8 −dendritic cells in the spleen. *J. Exp. Med.* **204**, 1653–1664 (2007).
19. Satpathy, A. T. et al. Notch2-dependent classical dendritic cells orchestrate intestinal immunity to attaching-and-effacing bacterial pathogens. *Nat. Immunol.* **14**, 937–948 (2013).
20. Fasnacht, N. et al. Specific fibroblastic niches in secondary lymphoid organs orchestrate distinct Notch-regulated immune responses. *J. Exp. Med* **211**, 2265–2279 (2014).
21. Franklin, R. A. et al. The cellular and molecular origin of tumor-associated macrophages. *Science* **344**, 921–925 (2014).
22. Gamrekelashvili, J. et al. Regulation of monocyte cell fate by blood vessels mediated by Notch signalling. Nature. *Communications* **7**, 71 (2016).
23. Gamrekelashvili, J. et al. Notch and TLR signaling coordinate monocyte cell fate and inflammation. *eLife* **9**, 902 (2020).
24. Fabre, T. et al. Identification of a broadly fibrogenic macrophage subset induced by type 3 inflammation. *Sci. Immunol.* **8**, eadd8945 (2023).
25. Reyfman, P. A. et al. Single-Cell Transcriptomic Analysis Of Human Lung Provides Insights Into The Pathobiology Of Pulmonary Fibrosis. *Am. J. Respiratory Crit. Care Med.* **199**, 1517–1536 (2019).
26. Adams, T. S. et al. Single-cell RNA-seq reveals ectopic and aberrant lung-resident cell populations in idiopathic pulmonary fibrosis. *Sci. Adv.* **6**, eaba1983 (2020).
27. Joshi, N. et al. A spatially restricted fibrotic niche in pulmonary fibrosis is sustained by M-CSF/M-CSFR signalling in monocyte-derived alveolar macrophages. *Eur. Respiratory J.* **55**, 1900646 (2020).
28. Wu, Y. et al. Therapeutic antibody targeting of individual Notch receptors. *Nature* **464**, 1052–1057 (2010).
29. Lafkas, D. et al. Therapeutic antibodies reveal Notch control of transdifferentiation in the adult lung. *Nature* **528**, 127–131 (2015).
30. Zhang, K. et al. Cutting edge: notch signaling promotes the plasticity of group-2 innate lymphoid cells. *J. Immunol.* **198**, 1798–1803 (2017).
31. Aran, D. et al. Reference-based analysis of lung single-cell sequencing reveals a transitional profibrotic macrophage. *Nat. Immunol.* **20**, 163–172 (2019).

32. Lavin, Y. et al. Tissue-resident macrophage enhancer landscapes are shaped by the local microenvironment. *Cell* **159**, 1312–1326 (2014).
33. Manno, G. L. et al. RNA velocity of single cells. *Nature* **560**, 494–498 (2018).
34. Boring, L. et al. Impaired monocyte migration and reduced type 1 (Th1) cytokine responses in C-C chemokine receptor 2 knockout mice. *J. Clin. Invest* **100**, 2552–2561 (1997).
35. Tsou, C.-L. et al. Critical roles for CCR2 and MCP−3 in monocyte mobilization from bone marrow and recruitment to inflammatory sites. *J. Clin. Invest* **117**, 902–909 (2007).
36. Tan, Y. & Cahan, P. SingleCellNet: a computational tool to classify single cell RNA-Seq data across platforms and across species. *Cell Syst.* **9**, 207–213.e2 (2019).
37. DeTomaso, D. & Yosef, N. Hotspot identifies informative gene modules across modalities of single-cell genomics. *Cell Syst.* **12**, 446–456.e9 (2021).
38. Jaitin, D. A. et al. Lipid-associated macrophages control metabolic homeostasis in a trem2-dependent manner. *Cell* **178**, 686–698.e14 (2019).
39. Schneider, C. et al. Frontline science: coincidental null mutation of Csf2rα in a colony of PI3Kγ − /− mice causes alveolar macrophage deficiency and fatal respiratory viral infection. *J. Leukoc. Biol.* **101**, 367–376 (2017).
40. Angelidis, I. et al. An atlas of the aging lung mapped by single cell transcriptomics and deep tissue proteomics. *Nat. Commun.* **10**, 1–17 (2019).
41. Remmerie, A. et al. Osteopontin expression identifies a subset of recruited macrophages distinct from kupffer cells in the fatty liver. *Immunity* **53**, 641–657.e14 (2020).
42. Sommerfeld, S. D. et al. Interleukin−36γ−producing macrophages drive IL-17−mediated fibrosis. *Sci. Immunol.* **4**, eaax4783 (2019).
43. Farbehi, N. et al. Single-cell expression profiling reveals dynamic flux of cardiac stromal, vascular and immune cells in health and injury. *eLife* **8**, e43882 (2019).
44. Peyser, R. et al. Defining the activated fibroblast population in lung fibrosis using single-cell sequencing. *Am. J. Resp. Cell Mol.* **61**, 74–85 (2019).
45. Strunz, M. et al. Alveolar regeneration through a Krt8+ transitional stem cell state that persists in human lung fibrosis. *Nat. Commun.* **11**, 3559 (2020).
46. Misharin, A. V., Morales-Nebreda, L., Mutlu, G. M., Budinger, G. R. S. & Perlman, H. Flow cytometric analysis of macrophages and dendritic cell subsets in the mouse lung. *Am. J. Respir. Cell Mol. Biol.* **49**, 130522202035005 (2013).
47. Jin, S. et al. Inference and analysis of cell-cell communication using CellChat. *Nat. Commun.* **12**, 1088 (2021).
48. Ramachandran, P. et al. Resolving the fibrotic niche of human liver cirrhosis at single-cell level. *Nature* **575**, 512–518 (2019).
49. Xiong, D., Wang, Y. & You, M. A gene expression signature of TREM2hi macrophages and γδ T cells predicts immunotherapy response. *Nat. Commun.* **11**, 5084 (2020).
50. Dinnon, K. H. et al. A mouse-adapted model of SARS-CoV-2 to test COVID-19 countermeasures. *Nature* **586**, 560–566 (2020).
51. Guilliams, M. & Svedberg, F. R. Does tissue imprinting restrict macrophage plasticity? *Nat. Immunol.* **22**, 118–127 (2021).
52. Theobald, H. et al. Apolipoprotein E controls Dectin-1-dependent development of monocyte-derived alveolar macrophages upon pulmonary β-glucan-induced inflammatory adaptation. *Nat. Immunol.* 1–13 https://doi.org/10.1038/s41590-024-01830-z. (2024).
53. Daemen, S. et al. Dynamic shifts in the composition of resident and recruited macrophages influence tissue remodeling in NASH. *Cell Rep.* **34**, 108626 (2021).
54. Sun, T. et al. TAZ is required for lung alveolar epithelial cell differentiation after injury. *JCI Insight* **4**, e128674 (2019).
55. Blaauboer, M. E. et al. Novel combination of collagen dynamics analysis and transcriptional profiling reveals fibrosis-relevant genes and pathways. *Matrix Biol.* **32**, 424–431 (2013).
56. Gardner, J. L. et al. Measurement of liver collagen synthesis by heavy water labeling: effects of profibrotic toxicants and antifibrotic interventions. *Am. J. Physiol. -Gastrointest. Liver Physiol.* **292**, G1695–G1705 (2007).
57. Case, J. B., Bailey, A. L., Kim, A. S., Chen, R. E. & Diamond, M. S. Growth, detection, quantification, and inactivation of SARS-CoV-2. *Virology* **548**, 39–48 (2020).
58. Li, B. et al. Cumulus provides cloud-based data analysis for large-scale single-cell and single-nucleus RNA-seq. *Nat. Methods* **17**, 793–798 (2020).
59. Gaublomme, J. T. et al. Nuclei multiplexing with barcoded antibodies for single-nucleus genomics. *Nat. Commun.* **10**, 2907 (2019).
60. Kotliarov, Y. et al. Broad immune activation underlies shared set point signatures for vaccine responsiveness in healthy individuals and disease activity in patients with lupus. *Nat. Med.* **26**, 618–629 (2020).
61. Bredikhin, D., Kats, I. & Stegle, O. MUON: multimodal omics analysis framework. *Genome Biol.* **23**, 42 (2022).
62. Wolf, F. A., Angerer, P. & Theis, F. J. SCANPY: large-scale single-cell gene expression data analysis. *Genome Biol.* **19**, 15 (2018).
63. Korsunsky, I. et al. Fast, sensitive and accurate integration of single-cell data with Harmony. *Nat. Methods* **16**, 1289–1296 (2019).
64. Bergen, V., Lange, M., Peidli, S., Wolf, F. A. & Theis, F. J. Generalizing RNA velocity to transient cell states through dynamical modeling. *Nat. Biotechnol.* **38**, 1408–1414 (2020).
65. Travaglini, K. J. et al. A molecular cell atlas of the human lung from single-cell RNA sequencing. *Nature* **587**, 619–625 (2020).

Acknowledgements

This study was funded by Genentech/Roche, NIH grant R01AI157155 (M.L. and M.S.D), by the Swiss National Science Foundation (320030-228477)(C.S.), and the Peter Hans Hofschneider Professorship for Molecular Medicine (C.S.). A.L. was funded by a Leopoldina Postdoctoral Fellowship (LPDS 2022-07). We are grateful to all members of the Andrey S. Shaw and Andy C. Chan labs at Genentech for fruitful discussions concerning this project. Preliminary studies in collaboration with A. Jovičić, D. Lafkas, and L. Riol Blanco labs were instrumental in starting this project. We thank the team of the Flow Cytometry Core at Genentech for support of FACS sorting. Furthermore, we are especially grateful to W. Ortiz and all members of the animal facility for all their help and hard work in ensuring animal welfare.

Author contributions

M.C.T. and M.N. conceived the project and proposed it to A.S.S. M.C.T. and M.N. designed and performed experiments. S.P.M. conceived and performed computational analyses. Animal experiments were performed in collaboration with J.J.H, V.S.G., B.K., and S.A. Bleomycin-induced fibrosis experiments were designed in collaboration with H.Br. and performed by A.W., A.A, S.J., and A.R. Histology analyses were performed by J.D.W., C.D.A., and H.Be. MA-10 viral work was performed at Washington University by M.L., under supervision of M.S.D. AM transplant experiments were designed with C.S. and performed by A.L. and B.C. at the University of Zurich. J.La., and J.Lu., ran the 10x platform under the supervision of M. De S., S.Da, and Z.M. M. De S., S.Da, and Z.M. also contributed by co-designing single-cell RNA sequencing experiments. S.Du. contributed to computational analyses. M.N. and A.S.S. supervised the project. M.C.T. and S.P.M. contributed equally to this work. M.C.T., S.P.M., A.S.S., and M.N. wrote the paper with suggestions from the authors.

Competing interests

M.C.T., S.P.M., A.W., A.A., J.D.W., J.La, J.J.H., V.S.G., M. De S. B.K., S.A., J. Lu, S.J., A.R., H.B., C.D.A., S.Da, Z.M., H.B., S.Du, A.S.S., and M.N. are

employees of Genentech/Roche. The remaining authors declare no other competing interests.

Additional information

Supplementary information The online version contains supplementary material available at https://doi.org/10.1038/s41467-024-53700-9.

Correspondence and requests for materials should be addressed to Sandra P. Melo, Andrey S. Shaw or Maximilian Nitschké.

Peer review information *Nature Communications* thanks Shigeyuki Shichino and the other, anonymous, reviewer(s) for their contribution to the peer review of this work. A peer review file is available.

Reprints and permissions information is available at http://www.nature.com/reprints

---

[1]Department of Cancer Immunology, Genentech Research and Early Development, South San Francisco, CA 94080, USA. [2]Department of Bioinformatics, Genentech Research and Early Development, South San Francisco, CA 94080, USA. [3]Department of Translational Immunology, Genentech Research and Early Development, South San Francisco, CA 94080, USA. [4]Department of Medicine, Washington University School of Medicine, St Louis, MO 63110, USA. [5]Department of Research Pathology, Genentech Research and Early Development, South San Francisco, CA 94080, USA. [6]Department of Proteomic and Genomic Technologies, Genentech Research and Early Development, South San Francisco, CA 94080, USA. [7]Department of Physiology, University of Zürich, Zürich, Switzerland. [8]Department of Research Biology, Genentech Research and Early Development, South San Francisco, CA 94080, USA. [9]Department of Molecular Microbiology Washington University School of Medicine, St Louis, MO 63110, USA. [10]Department of Pathology & Immunology, Washington University School of Medicine, St Louis, MO 63110, USA. [11]These authors contributed equally: Mayra Cruz Tleugabulova, Sandra P. Melo.
✉e-mail: melocars@gene.com; shawa6@gene.com; nitschkm@gene.com